SPECIAL
PECAN
COLLECTION

Multiscale Processes Enabling the Longevity and Daytime Persistence of a Nocturnal Mesoscale Convective System

Manda B. Chasteen

Cooperative Institute for Mesoscale Meteorological Studies, and School of Meteorology, University of Oklahoma, and NOAA/OAR/National Severe Storms Laboratory, Norman, Oklahoma

Steven E. Koch

NOAA/OAR/National Severe Storms Laboratory, and School of Meteorology, University of Oklahoma, Norman, Oklahoma

David B. Parsons

School of Meteorology, University of Oklahoma, Norman, Oklahoma

(Manuscript received 28 June 2018, in final form 24 November 2018)

ABSTRACT

Nocturnal mesoscale convective systems (MCSs) frequently develop over the Great Plains in the presence of a nocturnal low-level jet (LLJ), which contributes to convective maintenance by providing a source of instability, convergence, and low-level vertical wind shear. Although these nocturnal MCSs often dissipate during the morning, many persist into the following afternoon despite the cessation of the LLJ with the onset of solar heating. The environmental factors enabling the postsunrise persistence of nocturnal convection are currently not well understood. A thorough investigation into the processes supporting the longevity and daytime persistence of an MCS was conducted using routine observations, RAP analyses, and a WRF-ARW simulation. Elevated nocturnal convection developed in response to enhanced frontogenesis, which quickly grew upscale into a severe quasi-linear convective system (QLCS). The western portion of this QLCS reorganized into a bow echo with a pronounced cold pool and ultimately an organized leading-line, trailing-stratiform MCS as it moved into an increasingly unstable environment. Differential advection resulting from the interaction of the nocturnal LLJ with the topography of west Texas established considerable heterogeneity in moisture, CAPE, and CIN, which influenced the structure and evolution of the MCS. An inland-advected moisture plume significantly increased near-surface CAPE during the nighttime over central Texas, while the environment over southeastern Texas abruptly destabilized following the commencement of surface heating and downward moisture transport. The unique topography of the southern plains and the close proximity to the Gulf of Mexico provided an environment conducive to the postsunrise persistence of the organized MCS.

1. Introduction

Nocturnal mesoscale convective systems (MCSs) frequently occur over the Great Plains region of the United States (e.g., Kincer 1916; Means 1952; Wallace 1975; Fritsch et al. 1986; Carbone and Tuttle 2008) and are often elevated in that they exclusively ingest conditionally unstable air located above either a nocturnal inversion or a low-level frontal inversion (e.g., Maddox 1980, 1983; Corfidi 2003; Moore et al. 2003). This elevated instability, or CAPE, is generally supported by the poleward advection of high equivalent potential temperature (θ_e) air by a nocturnal low-level jet (LLJ; Fritsch and Maddox 1981; Maddox 1983). The LLJ may interact with a surface front to provide a focus for convection initiation (CI; Maddox 1983; Trier and Parsons 1993; Moore et al. 2003) or support CI in the absence of a surface boundary (Wilson and Roberts 2006; Pu and Dickinson 2014; Reif and Bluestein 2017; Gebauer et al. 2018).

Daytime MCSs are typically maintained by the regeneration of convective cells at the leading edge of a

Corresponding author: Manda B. Chasteen, manda.chasteen@ou.edu

cold pool (Rotunno et al. 1988), whereas nocturnal MCSs may be maintained or aided by a bore or gravity wave (e.g., Koch et al. 2008a; Parker 2008; Schumacher 2009; French and Parker 2010; Marsham et al. 2011; Blake et al. 2017). Furthermore, owing to spatiotemporal heterogeneity within the environment, different portions of a nocturnal MCS may be maintained by both cold pool and gravity wave mechanisms simultaneously (e.g., Schumacher 2015). Additionally, strong dynamical forcing associated with mature convection may be sufficient to lift conditionally unstable air within the near-surface stable layer to its level of free convection (LFC), enabling nocturnal convection to remain surface based (e.g., Parker 2008; Nowotarski et al. 2011; Billings and Parker 2012). The degree to which nocturnal convection is surface based is often uncertain and thus creates complications for forecasters, who may underestimate the severe wind and tornado threats associated with these systems (Horgan et al. 2007; Corfidi et al. 2008).

Parker (2008) and French and Parker (2010) utilized idealized simulations to describe how initially surface-based convection may become elevated in the presence of a stabilizing environment. However, fewer studies have explicitly examined how nocturnal convection responds to a destabilizing environment after sunrise. Marsham et al. (2011) documented elevated convection that developed near the terminus of the LLJ and triggered both gravity waves and bores, which initiated subsequent convection. During the morning, this elevated convection evolved into a surface-based MCS. Trier et al. (2011) examined this case using a WRF-ARW simulation and found that mesoscale processes were important for conditioning the inflow environment of the MCS and that the system lacked a well-defined cold pool until midmorning, which suggests that it had been maintained via elevated convergence throughout the night. Moreover, this study found that insolation did not significantly impact the strength of the convection until the system had become surface based, which led to the dominance of the cold pool.

Hane et al. (2008) conducted a 5-yr climatology of morning MCSs over the southern Great Plains and found that 28% remained steady or strengthened during the late morning and persisted into the afternoon. Despite this, the environmental factors responsible for such daytime persistence are currently not well understood. Hane et al. (2008) found that the movement of convection in tandem with a synoptic-scale disturbance did not increase the likelihood of daytime persistence despite the fact that these disturbances often played a role in CI. However, Gale et al. (2002) noted that MCSs over the Midwest tended to dissipate once

they were no longer supported by an LLJ, which may be the result of diminished CAPE and/or vertical wind shear.

We present herein an investigation into how multiscale processes and environmental heterogeneity influenced the development and evolution of an initially elevated, nocturnal MCS that persisted into the following afternoon as a surface-based system. Section 2 overviews the MCS and the synoptic environment in which it developed, and section 3 details the early evolution of the observed convection. A description of the WRF-ARW simulation used in this study is presented in section 4. Processes related to the LLJ and its interaction with topography are discussed in section 5. The influences of environmental heterogeneity and solar heating on the convective evolution are presented in section 6. Finally, a summary of this study and proposed avenues for future research are found in section 7.

2. Case description

Two convective clusters developed in central Oklahoma at approximately 0300 UTC[1] 6 October 2014. These clusters quickly grew upscale into a quasi-linear convective system (QLCS), and the western portion of the system (hereafter QLCS-W) reorganized into a bow echo and ultimately a leading-line, trailing-stratiform (LLTS) MCS (Fig. 1). Convection associated with this MCS persisted for more than 18 h and traversed more than 800 km before moving over the Gulf of Mexico. This event produced 21 severe wind and 21 severe hail reports between 0355 and 1725 UTC, and an EF1 tornado was reported in eastern Oklahoma just after 0600 UTC.

The timing, persistence, and severity of this event were poorly anticipated by both operational convective-allowing models and the Storm Prediction Center. For example, the 0000 UTC 6 October 2014 initialization of the High-Resolution Rapid Refresh (HRRR; Benjamin et al. 2016) model depicted CI in central Oklahoma, but failed to capture the upscale growth into a long-lived MCS (not shown). The propensity for numerical models to poorly depict the initiation and longevity of nocturnal convection has been discussed by several studies (e.g., Surcel et al. 2010; Kain et al. 2013; Pinto et al. 2015), and significant work is currently ongoing to improve forecasts of nocturnal convection as part of the recent Plains Elevated Convection at Night (PECAN) field campaign (Geerts et al. 2017).
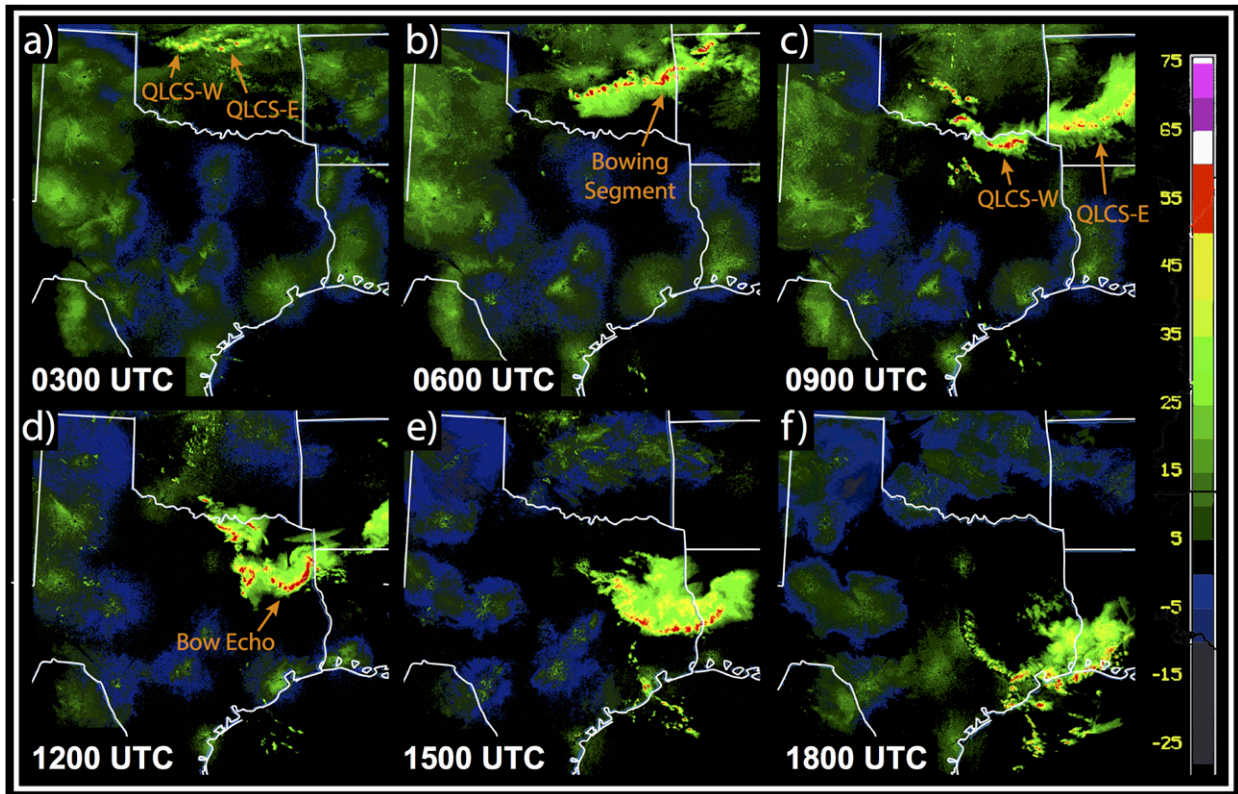
---

[1] LST = UTC − 6 h.

FIG. 1. Composite NEXRAD radar reflectivity (dBZ) for (a) 0300, (b) 0600, (c) 0900, (d) 1200, (e) 1500, and (f) 1800 UTC 6 Oct 2014.

Environmental overview

The MCS discussed herein materialized within a synoptically active environment typical of events occurring outside of the traditional warm season. During the daytime, an east–west temperature gradient had developed over the southern plains, and a surface low and dryline were located over the Edwards Plateau region of west Texas at 0200 UTC (Fig. 2). A quasi-stationary front, which was characterized primarily by a pronounced wind shift and low-level moisture gradient, extended northeastward from the low pressure center into central Oklahoma. Additionally, an extensive radar fine line had moved into northern Oklahoma, which was associated with a northwesterly wind surge accompanying a surface cold front that had been reinforced by convective outflow. As shown in the RAP analysis, this cold front propagated southeastward with time in tandem with an upper-level short-wave trough embedded within northwesterly flow (Figs. 3a,b).

A southerly nocturnal LLJ (e.g., Blackadar 1957; Whiteman et al. 1997) had begun to develop over the southern Great Plains by 0300 UTC (Fig. 3a), which advected moisture northward into central Oklahoma.

As the cold front approached the region of warm, moist air supported by the LLJ, strong northerly flow within the cold air mass acted in tandem with the increasing potential temperature gradient to enhance horizontal frontogenesis[2] at 925 hPa (Figs. 3c,d). The cold front ultimately merged with the quasi-stationary front, and frontogenetical forcing for ascent in the presence of high-θ_e air supported by the LLJ seemingly led to CI within the 13-km RAP analyses by 0400 UTC (not shown).

As previously stated, the two convective clusters had begun to develop by 0300 UTC (Fig. 1a): the western cluster (i.e., QLCS-W) formed along the observed surface cold front, but to the north of the quasi-stationary front, and the eastern cluster (i.e., QLCS-E) formed along the quasi-stationary front prior to the frontal merger. At 0300 UTC, the RAP analysis depicted most-unstable CAPE (CIN) values, which are calculated by lifting the highest θ_e parcel located within the lowest

---

[2] The assumptions regarding horizontal Petterssen frontogenesis exclude vertical tilting and diabatic processes, which may have been relevant above ground (i.e., at 925 hPa) and in the presence of precipitation.
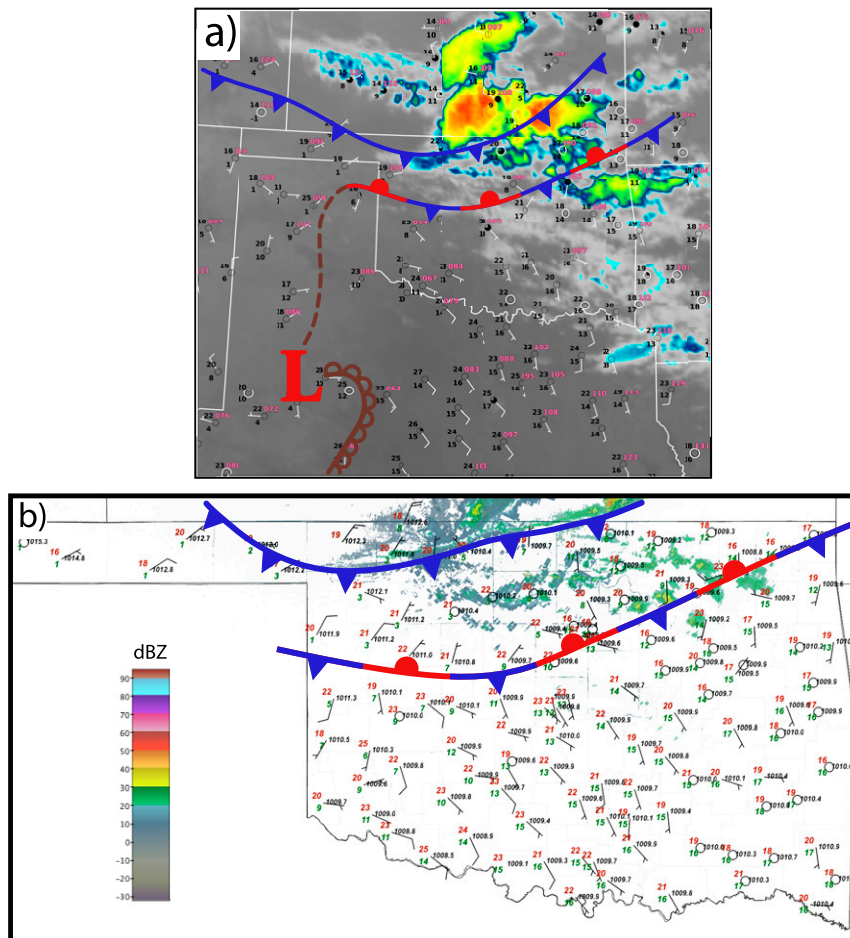
0200 UTC

FIG. 2. Surface observations from (a) ASOS locations overlaid with *Geostationary Operational Environmental Satellite-13* (*GOES-13*) 10.7-μm IR satellite imagery and (b) Oklahoma Mesonet locations overlaid with NEXRAD radar reflectivity (dBZ) from Vance AFB, Oklahoma (KVNX), valid at 0200 UTC 6 Oct 2014. Warmer colors in (a) denote colder brightness temperatures. The quasi-stationary front, dryline, and cold front are illustrated using standard notation, and the low pressure center is indicated by the red "L." An extensive radar fine line is collocated with the cold front.

300 hPa, that were generally greater than 1000 J kg^{-1} (less than 50 J kg^{-1}) in central Oklahoma (Figs. 4a,b). The corresponding RAP sounding from Kingfisher, Oklahoma—located to the north of the quasi-stationary front near the observed CI region for QLCS-W—exhibited a strong nocturnal inversion and dry lower troposphere with an overlying moist layer centered at approximately 600 hPa (Fig. 4c). Moreover, the most pronounced layer of potential instability was located above ~650 hPa, which would be omitted from the most-unstable CAPE calculation owing to 1) the presence of a higher θ_e parcel at 950 hPa, and 2) its location above the lowest 300 hPa of the profile. The vertical displacement required for a parcel originating at some level (z_0) to reach its LFC (z_{LFC}), given by

$$\Delta z_{LFC} = z_0 - z_{LFC}, \qquad (1)$$

can be used to better estimate the source layers for convective updrafts (e.g., Houston and Niyogi 2007). One should note that this method is subject to the fundamental assumptions behind parcel theory and therefore ignores the implications of layer lifting, which may enable low-level parcels to become unstable at lower heights as inversion layers aloft are weakened via ascent (Bryan and Fritsch 2000). Unlike the deemed "most-unstable parcel," which required $\Delta z_{LFC} \approx 3.5$ km, parcels within the elevated layer of potential instability required <1 km of lifting, which supported the development of the shallow elevated convection observed
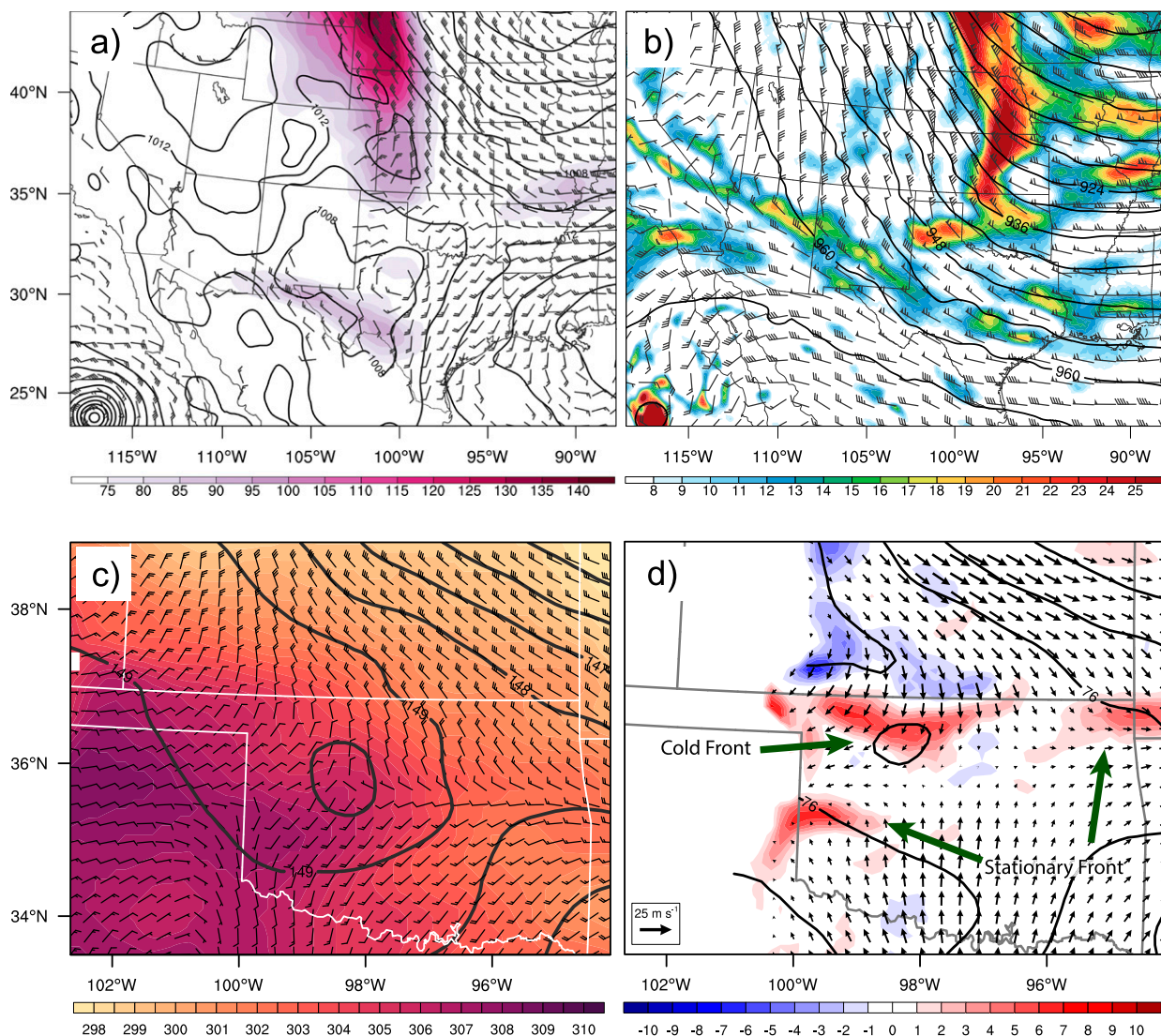
FIG. 3. Depiction of (a) 250-hPa wind speed (shaded; kt), 850-hPa wind barbs (half barb = 5, full barb = 10, pennant = 50 kt; 1 kt = 0.5144 m s^{-1}), and sea level pressure (contours; hPa), (b) 300-hPa absolute vorticity (ζ_a, shaded; $\times 10^{-5}$ s^{-1}), wind barbs (kt), and geopotential height (contours; dam), (c) 850-hPa potential temperature (shaded; K), geopotential height (contours; dam), and wind barbs (kt), and (d) 925-hPa Petterssen horizontal frontogenesis function [shaded; K (100 km $\times$ 3 h)$^{-1}$], geopotential height (contours; dam), and wind vectors (m s^{-1}) using the RAP analysis valid at 0300 UTC 6 Oct 2014.

ahead of the short-wave trough (Fig. 2). Although the Kingfisher sounding did not specifically support the development of deep convection, this observation is noteworthy because it alludes to the shortcomings associated with using most-unstable CAPE and CIN to forecast the general formation of elevated convection.

In contrast, the 0300 UTC RAP sounding from Norman, Oklahoma—located just south of the quasi-stationary front—was characterized by a low-level moist layer that was overlain by a midlevel dry layer, which collectively yielded a deep layer of elevated potential instability (Fig. 4d). While $\Delta z_{LFC} > 2$ km for much of the profile at this time, further destabilization within this

region likely occurred prior to CI owing to low-level moisture advection and ascent ahead of the approaching short-wave trough. As frontogenesis increased across central Oklahoma in association with the approaching cold front and subsequent frontal merger, strong mesoscale forcing for ascent within this destabilizing air mass would have fostered the development of deep, elevated convection. Additionally, the Norman RAP sounding was characterized by a 0–6-km bulk wind difference of 26.1 m s^{-1} and a corresponding deep-layer shear vector that was directionally invariant with height. Such a shear profile supported the development of a QLCS-type convective mode
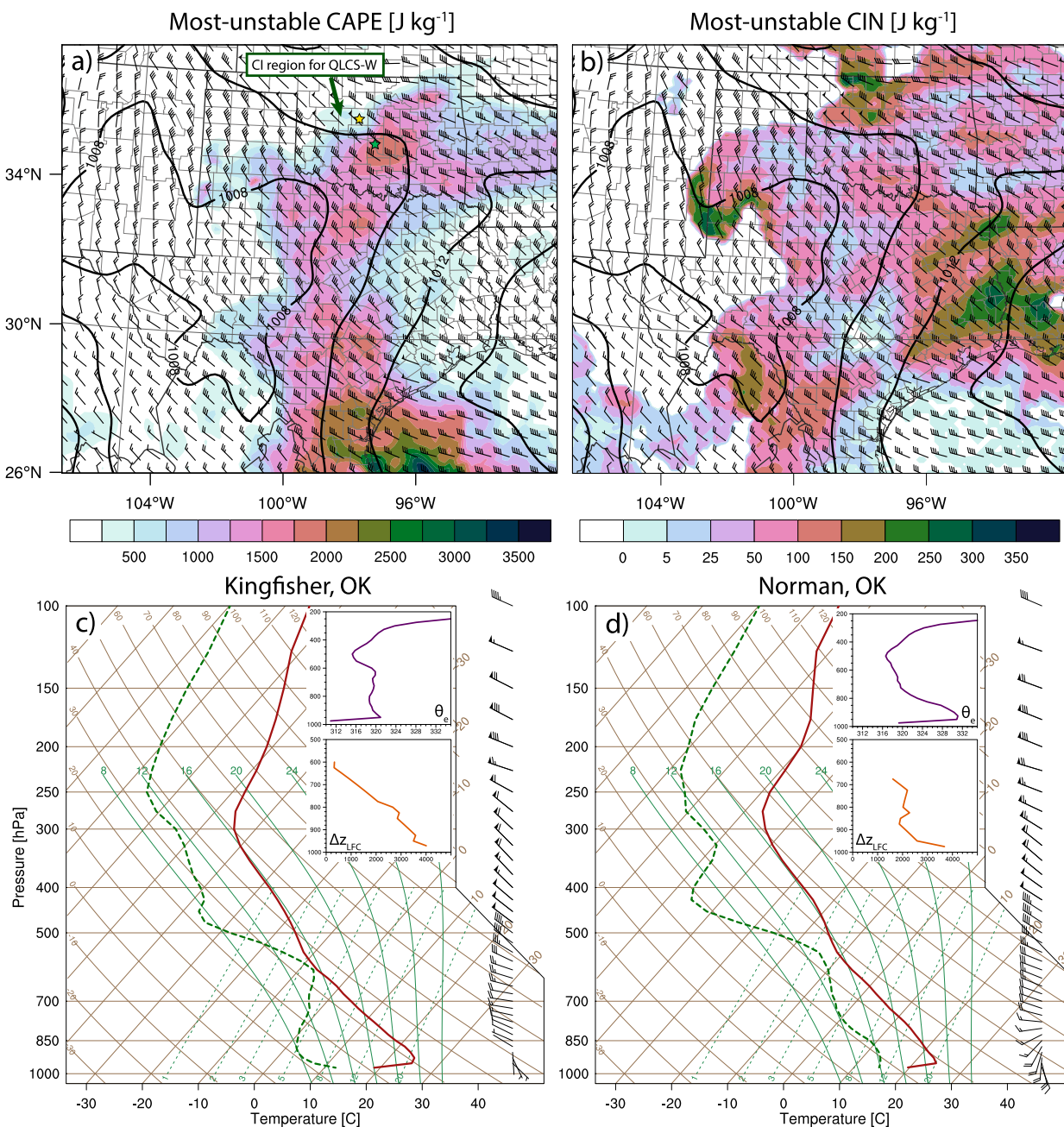
FIG. 4. RAP analysis depiction of (a) CAPE (shaded; J kg^{-1}) and (b) CIN (shaded; J kg^{-1}) for the most-unstable parcel within the lowest 300 hPa at 0300 UTC 6 Oct 2014. Sea level pressure (contours; hPa) and 1000–500-hPa bulk wind difference (barbs; kt) are also shown in (a) and (b). The corresponding RAP soundings for (c) Kingfisher, OK, and (d) Norman, OK, are depicted on the bottom. The sounding insets include profiles of θ_e (violet; K) and Δz_{LFC} (orange; m) for parcels located at various pressure levels (hPa). The yellow and green stars in (a) denote the locations of Kingfisher and Norman, respectively.

characterized by embedded circulations and bowing segments (Thompson et al. 2012).

3. Radar and Oklahoma Mesonet observations

The early convective evolution was examined using both NEXRAD (Crum and Alberty 1993) and Oklahoma

Mesonet (Brock et al. 1995) observations, which have a 5-min temporal resolution. Shortly after their development, both aforementioned convective clusters rapidly became invigorated as they moved southward into an increasingly unstable air mass and developed cold pools (Fig. 4). QLCS-W passed over the El Reno, Oklahoma,
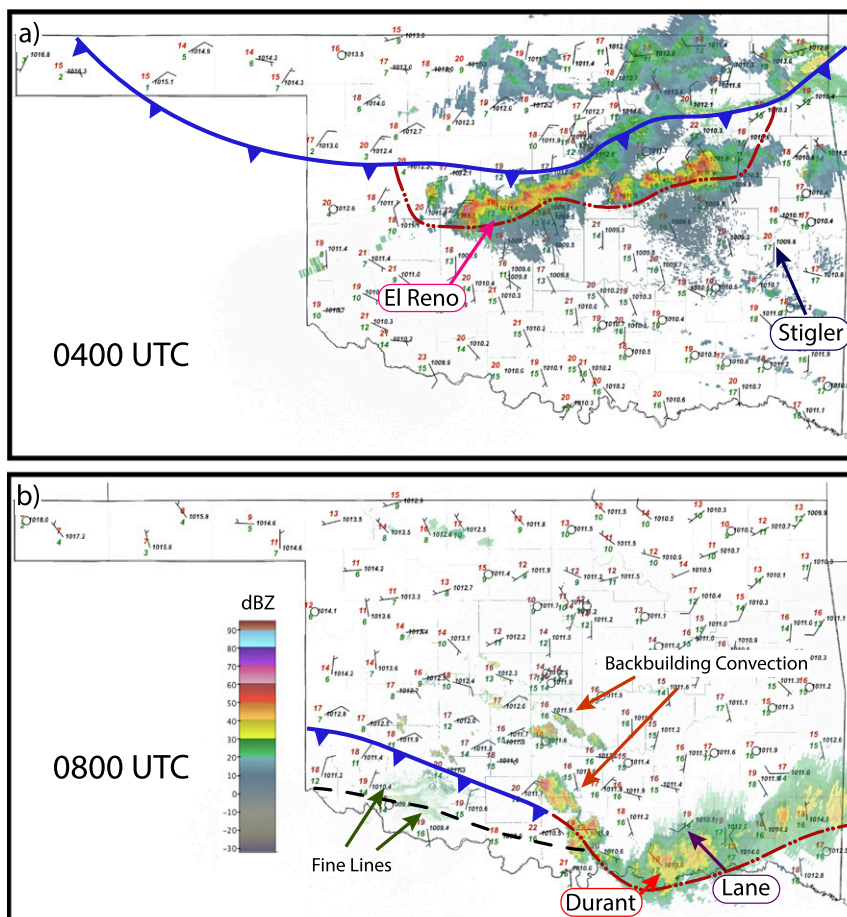
FIG. 5. As in Fig. 2b, but for (a) 0400 and (b) 0800 UTC. The cold front and outflow boundary are drawn with standard notation, and the dashed black line represents the location of the wind shift line associated with the bore front. NEXRAD radar reflectivity is a composite produced from the following radars: Vance AFB (KVNX), Oklahoma City (KTLX), Tulsa (KINX), Frederick (KFDR), OK, and Ft. Smith (KSRX), AR.

Mesonet site at approximately 0400 UTC, which was located just to the south of the quasi-stationary front (Figs. 5a, 6a). Temperature and pressure rises of 2.2°C and 1.7 hPa, respectively, and 20–30-kt wind gusts were observed during a 15-min period prior to the passage of the outflow boundary at 0405 UTC. These temporal signatures in the surface observations suggest that a bore may have been associated with QLCS-W early during its lifetime (e.g., Koch et al. 1991). Following this invigoration period, several individual cells within the two clusters acquired supercellular characteristics and produced severe wind and hail reports across central Oklahoma. At approximately 0601 UTC, an EF1 tornado formed from an intensifying mesovortex along the northern flank of a bowing segment within QLCS-E (Fig. 1b). The Mesonet site in Stigler, Oklahoma, which was impacted by the bowing segment and located approximately 48 km west of the location of the tornado,

observed a 3.6-hPa pressure jump coincident with 40-kt wind gusts and a 4°C temperature decrease (Fig. 6b); such surface signatures are consistent with the passage of a density current, which suggests that the dry midlevel air had fostered the development of a pronounced cold pool. QLCS-E, along with frontal convection that later developed in Arkansas, continued to move southeastward with time along with the upper-level disturbance (Fig. 1c).

By 0800 UTC, the convection in southeastern Oklahoma that was associated with QLCS-W had split from QLCS-E and weakened considerably, and backbuilding convection (e.g., Schumacher and Johnson 2005; Keene and Schumacher 2013; Peters and Schumacher 2015) had developed behind the merged outflow–frontal boundary and a preceding wind-shift line (Fig. 5b). This wind-shift "line" was manifested as several parallel fine lines with horizontal wavelengths of approximately
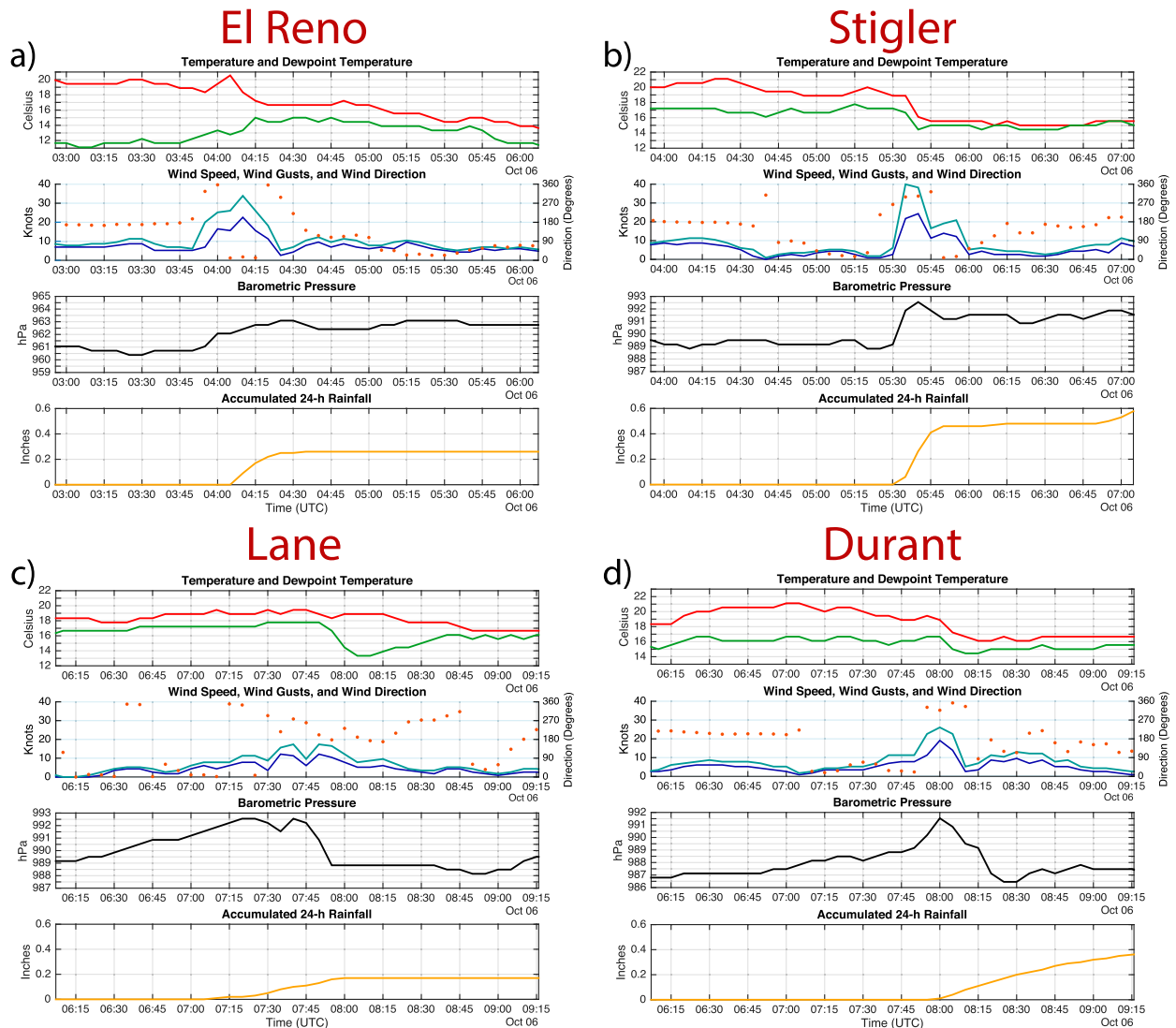
FIG. 6. Meteograms of 5-min surface observations taken at the Oklahoma Mesonet sites in (a) El Reno, (b) Stigler, (c) Lane, and (d) Durant, OK. The individual meteogram panels are (from top to bottom) temperature (red; °C) and dewpoint temperature (green; °C); wind speed (navy; kt), wind gusts (blue; kt), and wind direction (orange; degrees); altimeter pressure (black; hPa); and 24-h accumulated rainfall (orange; in.). Site locations are denoted in Fig. 5.

5–8 km, and surface warming was observed with its passage at several locations in southwestern Oklahoma. These fine lines were likely affiliated with a bore (e.g., Wilson and Roberts 2006; Koch et al. 2008a), and the ascent of warm, moist air over this bore and the trailing outflow–frontal boundary apparently led to backbuilding CI.

Unlike with the passage of QLCS-E at Stigler 90 min earlier, no distinct cold pool was observed at Lane, Oklahoma, as QLCS-W moved over the site after 0700 UTC (Fig. 6c). However, a wake low signature (Johnson and Hamilton 1988) was observed behind the convection, which had manifested as a 3.3-hPa pressure

decrease over a 10-min period coincident with substantial drying. A similar signature was detected at the Durant, Oklahoma, site after 0800 UTC, which was characterized by a 5-hPa pressure decrease over a 25-min period (Fig. 6d). Wake lows often develop within the stratiform region to the rear of weakening or dissipating convection, and previous studies have attributed their formation to a descending rear-inflow jet (RIJ) behind the convective line (e.g., Johnson and Hamilton 1988). Therefore, the development of a descending RIJ may have contributed to the subsequent reorganization of QLCS-W as it moved into northern Texas (Fig. 1). This idea is examined more fully in section 6a.
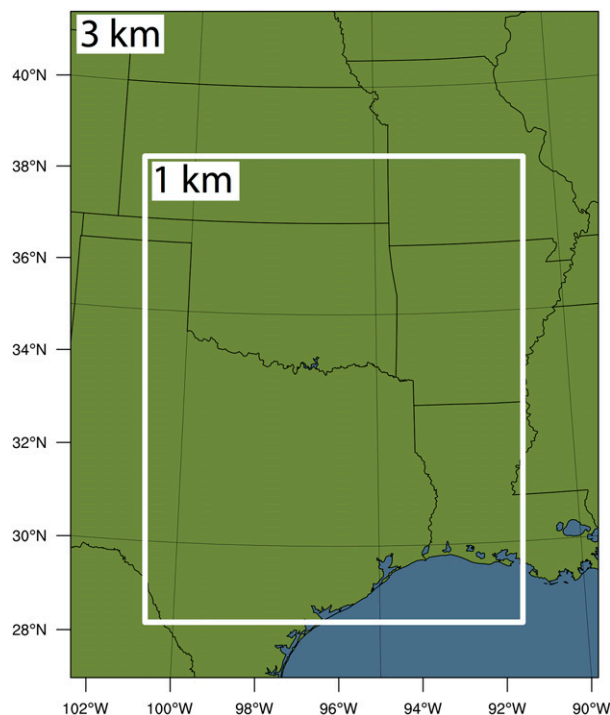
FIG. 7. The grid configuration used for the WRF-ARW simulation. The outer domain is characterized by a 3-km horizontal grid spacing, and the inner nest (encompassed by the white rectangle) is characterized by a 1-km horizontal grid spacing.

TABLE 1. WRF-ARW Model, version 3.6.1, configuration and physics parameterizations.

Configuration	Outer domain	Inner domain
Horizontal grid spacing	3 km	1 km
No. of grid points	420 × 530	901 × 1111
No. of vertical levels	100	100
Time step	3 s	1 s
ICs/BCs	13-km RAP	13-km RAP
Cumulus	None	None
PBL	MYNN level 2.5	MYNN level 2.5
Surface layer	Eta similarity	Eta similarity
LSM	Unified Noah	Unified Noah
Microphysics	Morrison	Morrison
Shortwave radiation	Dudhia	Dudhia
Longwave radiation	RRTM	RRTM

4. WRF simulation

a. Model configuration

To better understand how the MCS and its environment evolved, a 23-h simulation was conducted from 2100 UTC 5 October to 2000 UTC 6 October 2014 using version 3.6.1 of the WRF-ARW Model (Skamarock et al. 2008). Initial conditions (ICs) for atmospheric and soil fields were obtained from the 13-km RAP analysis valid at 2100 UTC (Benjamin et al. 2016), and the lateral boundary conditions (BCs) were updated hourly using the corresponding hourly RAP analyses. The simulations were run with convective-permitting grid spacings (i.e., no cumulus parameterization was employed), with two-way nested domains of $\Delta x = \Delta y = 3$ km (outer) and $\Delta x = \Delta y = 1$ km (inner), respectively (Fig. 7). All WRF analyses discussed herein were performed using the 1-km inner domain. A stretched vertical grid comprising 100 vertical levels below 30 hPa was utilized. The lowest grid point was located at approximately 14 m AGL, and the average Δz within the lowest 1 km was approximately 60 m in order to provide high vertical resolution within the stable PBL.

The parameterizations utilized in the simulation are summarized in Table 1. The Mellor–Yamada–Nakanishi–Niino (MYNN) level 2.5, TKE-based PBL scheme (Nakanishi

and Niino 2006, 2009) was used in tandem with the Eta surface layer scheme (Janjić 1996), which is based upon Monin–Obukhov similarity theory. The coupled Unified Noah LSM (Ek et al. 2003) was utilized to update the soil fields with time. Owing to the complex microphysical structure of MCSs and the importance of this structure to the internal dynamics of these systems, the double-moment Morrison microphysics parameterization (Morrison et al. 2009) was employed, which has been shown to produce realistic trailing-stratiform regions. This parameterization utilized a "hail-like" option for graupel, which previous studies (e.g., Adams-Selin et al. 2013) have shown to help mitigate the tendency for microphysics schemes to result in cold pools that are unrealistically too strong. Additionally, the employment of a hail-like microphysical class allowed for the depiction of more distinct convective cores (Bryan and Morrison 2012). Shortwave and longwave radiation were parameterized using the Dudhia (Dudhia 1989) and RRTM (Mlawer et al. 1997) schemes, respectively.

b. Verification of simulation and overview of the simulated MCS

The evolution of the WRF simulated radar reflectivity is shown in Fig. 8. In terms of reflectivity structure, the simulated MCS closely resembled the observed system during its later stages (i.e., after it had moved into Texas), but the early hours of the simulation were complicated by erroneous convection that formed in central Oklahoma shortly after initialization. The development of this convection was caused by persistent, regional errors in the low-level dewpoint field within the RAP ICs, which produced a localized region of CAPE > 2000 J kg^{-1} (Fig. 9) in central Oklahoma, as compared to approximately 433 J kg^{-1} observed by the Norman
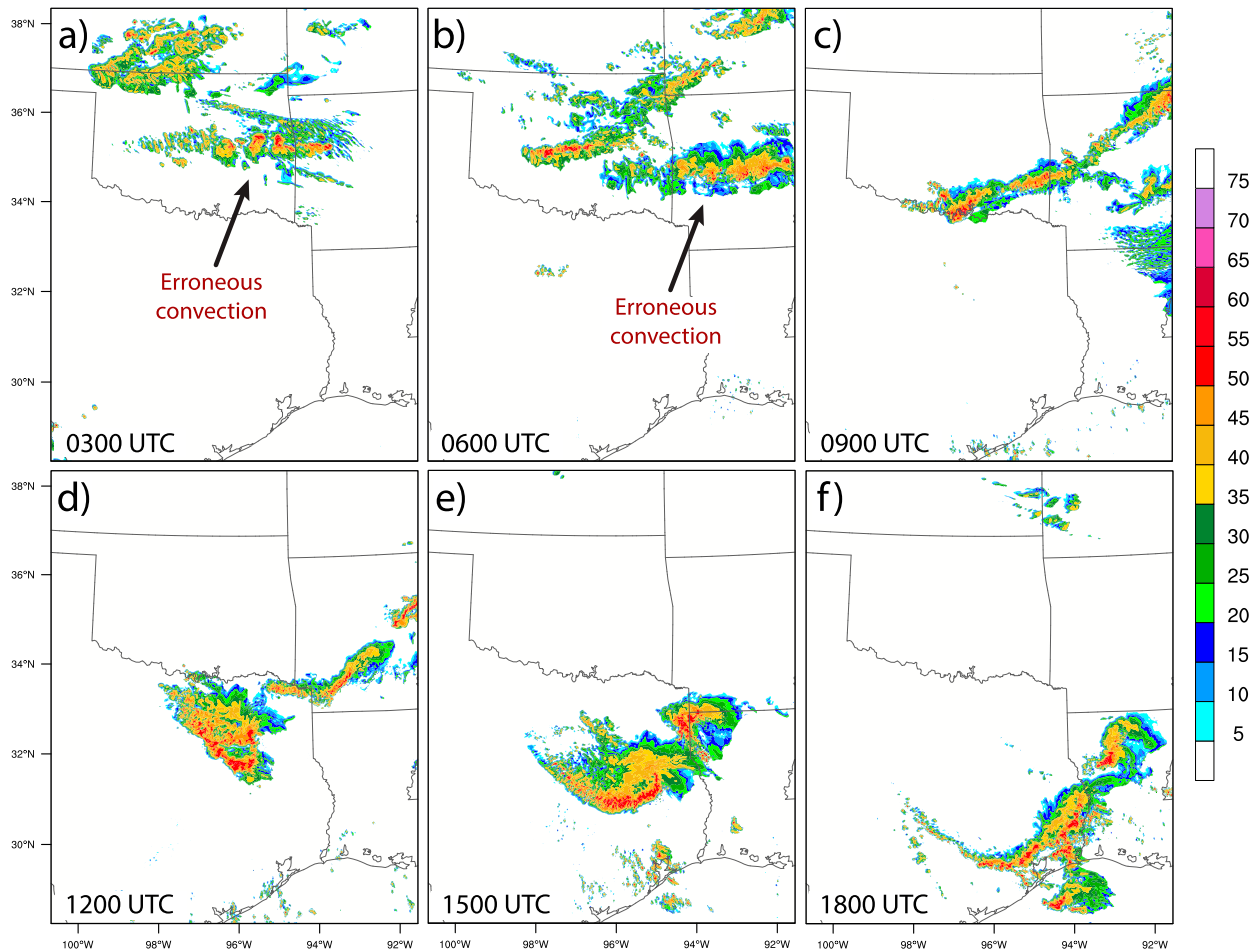
FIG. 8. Simulated radar reflectivity factor (dBZ; lowest model level) valid at (a) 0300, (b) 0600, (c) 0900, (d) 1200, (e) 1500, and (f) 1800 UTC 6 Oct 2014. The erroneously simulated MCS is denoted by the black arrow.

sounding 2 h later (not shown). These dewpoint errors resulted from an error in the dewpoint observation at the ASOS site in Shawnee, Oklahoma,[3] which was then ingested into the RAP model through its hourly data assimilation system (Benjamin et al. 2016). Unfortunately, the persistence of this error meant that other RAP initialization times (e.g., 2000 UTC, 2200 UTC) produced similar results. However, simulations that were initialized using other models (e.g., GFS and NAM) failed to produce a long-lived MCS.[4]

The erroneous convection had weakened by 0600 UTC and was absent in the simulation by 0900 UTC (Figs. 8b,c), but this system had produced a shallow cold pool over

central and southern Oklahoma, which impacted the initiation and early evolution of the MCS of interest. Despite the initial deficiency in the simulation, both the observed (Fig. 1c) and simulated convection (Fig. 8c) had split into two portions (i.e., QLCS-E and QLCS-W) by 0900 UTC, and the simulated QLCS-W had moved to the south of the erroneous outflow boundary and reorganized into a bow echo near the Oklahoma–Texas border. Additionally, backbuilding convection was evident in the WRF simulation by 0900 UTC, but was weaker and less extensive than in the observations. Because considerable heterogeneity in moisture and instability existed within the environment in this region (as is discussed in the following sections), this discrepancy may be attributed to a ~100–120-km westward bias in the location of the simulated bow echo, which likely resulted from the influence of the erroneous cold pool on the early convective evolution.

After the simulated convection had moved into Texas, it was subjected to low-level thermodynamic and wind profiles that were undisturbed by the prior erroneous

---

[3] Location shown in Fig. 9. When compared to the Oklahoma Mesonet site also located in Shawnee, the dewpoint reading at the ASOS was approximately 3°–5°C greater for several hours.

[4] The sensitivity of the simulated convection to IC differences is beyond the scope of this paper, and the reader is directed to Chasteen (2017) for further discussion.
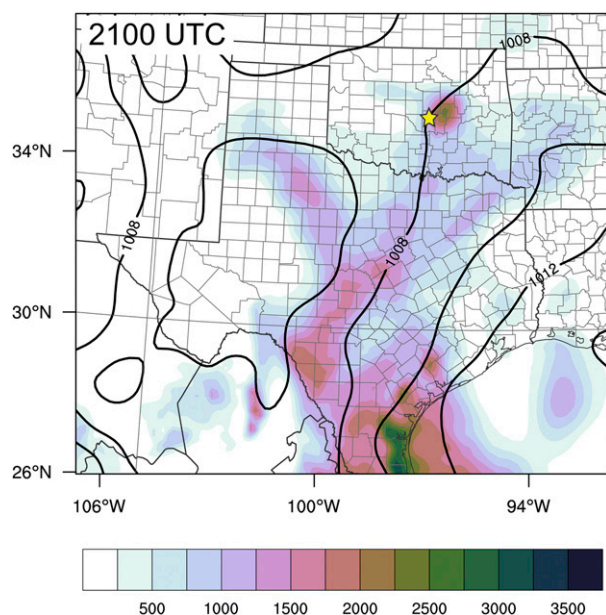
FIG. 9. RAP analysis depiction of surface-based CAPE (shaded; J kg^{-1}) and sea level pressure (contours; hPa) at 2100 UTC 5 Oct 2014. The yellow star denotes the location of Shawnee, OK.

convection over Oklahoma and thus behaved comparably to the observed convection after approximately 0900 UTC. Such consistency suggests that insight into the processes responsible for its reorganization into a LLTS MCS and persistence after sunrise can be gleaned from the WRF simulation despite the initial discrepancies. Therefore, the following discussion will focus primarily on the WRF simulation.

5. LLJ evolution and establishment of environmental heterogeneity

We next describe how processes influenced by the nocturnal LLJ led to the establishment of environmental heterogeneity, which ultimately influenced the convective structure and evolution.

a. Background on the LLJ

The preferred frequency of the southerly nocturnal LLJ over the Great Plains has been well documented (e.g., Bonner 1968; Whiteman et al. 1997; Song et al. 2005), and its formation has been attributed to both the inertial oscillation (Blackadar 1957) and baroclinicity arising from differential heating and cooling over sloping terrain (Holton 1967). Recent analytical studies (e.g., Shapiro and Fedorovich 2009; Du and Rotunno 2014; Shapiro et al. 2016) have attempted to unify these theories, and the resultant LLJs from such an inertia–gravity oscillation (not to be confused with inertia–gravity

waves) have structures and evolutions consistent with observations and climatology.

However, such 1D analytical studies do not account for all processes that may arise owing to differential heating over sloping terrain. For example, Gebauer et al. (2018) recently described how differential heating over the Great Plains can promote zonal variability in the depth of the daytime convective PBL, which subsequently influences the depth and strength of the nocturnal LLJ. These horizontal variations in baroclinicity and PBL depth promote stronger, height-veering LLJs over the higher terrain, which also veer with time owing to the inertial oscillation. LLJs with spatially heterogeneous structures are responsible for differential thermal and moisture advection and have been shown to yield eastward-moving regions of elevated convergence that may lead to the development of north–south-oriented lines of convection (Reif and Bluestein 2017; Gebauer et al. 2018). Additionally, 3D terrain variations (e.g., regional plateaus), which may influence the low-level thermodynamic and wind fields, are neglected by the aforementioned analytical studies.

b. Moisture plume and development of capping inversion

As previously described, an east–west temperature gradient had developed over the southern plains throughout the day as a result of elevated heating over the Edwards Plateau. During the evening, the onset of the inertia–gravity oscillation induced southeasterly upslope flow over central Texas (Fig. 2a), and the low pressure center intensified as it moved northeastward with time. Baroclinicity arising from horizontal variations in daytime heating and PBL depth (Fig. 10a) supported the development of a spatially heterogeneous, height-veering LLJ, which was strongest to the east of the low pressure center along the sloping terrain of the Balcones Escarpment (location denoted in Fig. 11a). The strongest winds within the LLJ were located at approximately 400–500 m AGL (Figs. 10b,c), which provided considerable moisture advection (Figs. 10d–f) and led to a temporal increase in elevated CAPE over central Texas (Figs. 10g–i). By 0600 UTC, two pronounced regions of elevated CAPE were evident: 1) a region located between 1.5 and 4 km MSL and centered at $x \approx 250$ km, which was associated with northeastward moisture advection as the LLJ veered with height, and 2) a region located between 1 and 2 km MSL and $x = 200$–500 km, which was the result of poleward moisture advection and ascent as the LLJ veered with time (Fig. 10h).

The simulated mesoscale environment in this particular case had a rather unique evolution in that surface-based
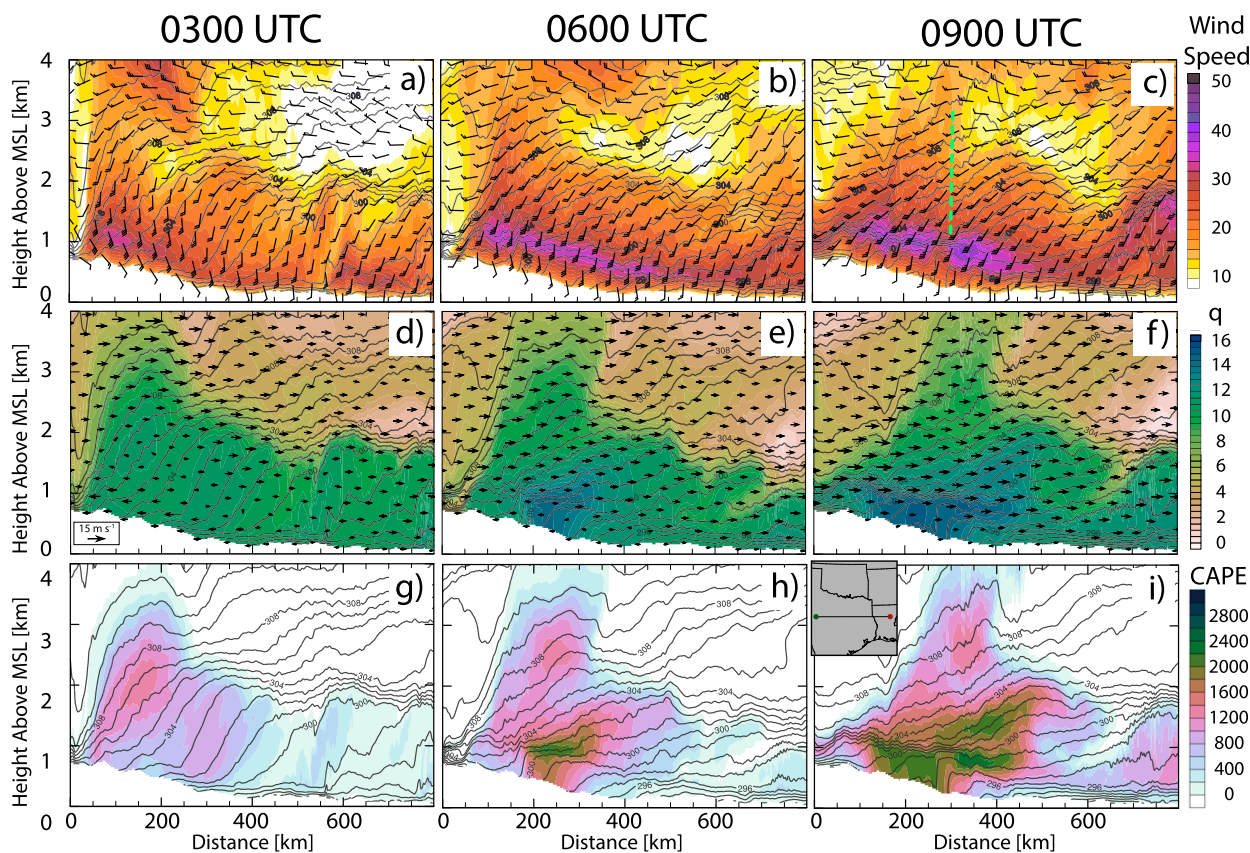
FIG. 10. West–east vertical cross sections of (top) wind speed (shaded; kt), θ (gray contours; K), and wind barbs (kt) for (a) 0300, (b) 0600, and (c) 0900 UTC; (middle) water vapor mixing ratio (shaded; g kg^{-1}), θ (gray contours; K), and zonal winds (vectors; m s^{-1}) for (d) 0300, (e) 0600, and (f) 0900 UTC; and (bottom) CAPE (shaded; J kg^{-1}) and θ (gray contours; K) for (g) 0300, (h) 0600, and (i) 0900 UTC 6 Oct 2014. The dashed green line in (c) depicts the approximate location of an eastward-moving region of elevated convergence. The cross-sectional path (where the green circle corresponds to 0-km distance on the x axis) is overlaid with panel (i).

CAPE also increased substantially throughout the night within a relatively narrow corridor paralleling the Balcones Escarpment (Figs. 10, 11). Such a stark increase in surface-based CAPE was peculiar because the formation of a nocturnal inversion, which generally precedes the development of an LLJ, typically decouples the near-surface air from the layer of greater instability aloft and also inhibits the downward transport of moisture advected northward by the LLJ until after sunrise. This corridor of high surface-based CAPE developed in association with the inland advancement of a low-level moisture plume originally located over the Gulf of Mexico (Figs. 11a–f), which was characterized by high relative humidity, weak near-surface stability, low-level turbulent mixing, and enhanced surface winds. This moisture plume was evident in the ASOS observations at 0900 and 1200 UTC as the northward protrusion of high dewpoint temperatures and dense low-level cloud cover located over central Texas (Figs. 12a,b). Moreover, enhanced surface winds were observed within the

moisture plume, but the observed wind speeds were ~5 kt slower than the simulated 10-m wind speeds over much of the region (not shown). This discrepancy suggests that the MYNN PBL scheme may have produced too much turbulence within the moisture plume owing to the presence of strong vertical wind shear and weak static stability.

Characteristics of nocturnal moisture plumes were described by Hu and Xue (2016), who found that they often move as far northward as Dallas, Texas, following the onset of the LLJ. Consistent with their findings, the simulated moisture plume described herein had an initial structure resembling that of a sea-breeze density current (not shown), which broke down following the development of the LLJ. After sunset, the LLJ first developed within the moisture plume near the Texas Gulf Coast, and its leading edge advanced nearly 300 km inland by 0300 UTC. Over time, the LLJ veered in response to the inertia–gravity oscillation, which caused the plume to advance northward parallel to and along
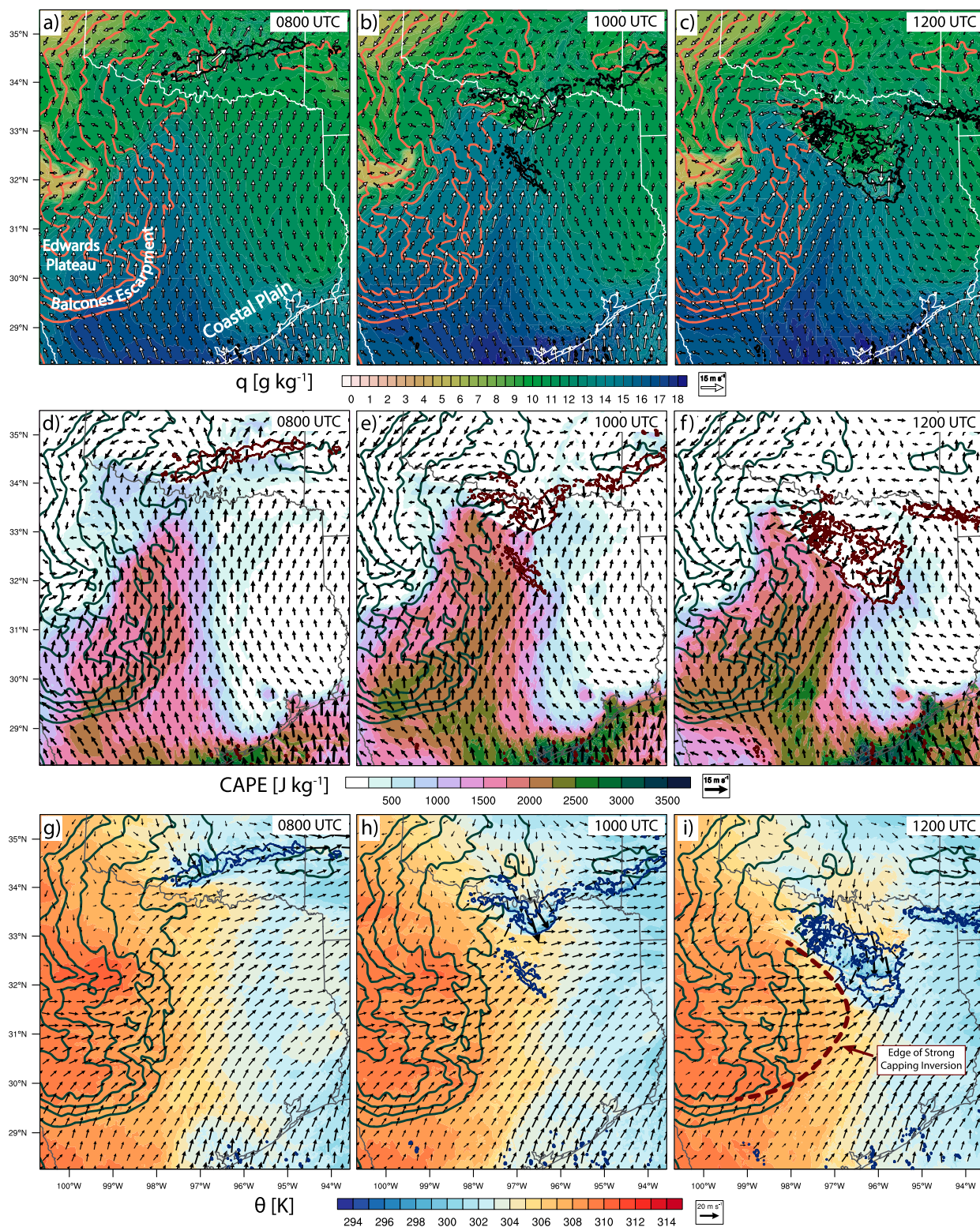
FIG. 11. WRF depiction of (top) surface water vapor mixing ratio (shaded; g kg^{-1}), 0-dBZ radar reflectivity (black contours), terrain height (orange contours; every 100 m between 300 and 700 m), and surface wind vectors (m s^{-1}) for (a) 0800, (b) 1000, and (c) 1200 UTC; (middle) surface-based CAPE (shaded; J kg^{-1}), 0-dBZ radar reflectivity (red contours), terrain height (green contours; every 100 m between 300 and 700 m), and surface wind vectors (m s^{-1}) for (d) 0800, (e) 1000, and (f) 1200 UTC; and (bottom) 1.5-km θ (shaded; K), 0-dBZ radar reflectivity (blue contours), terrain height (green contours; every 100 m between 300 and 700 m), and 1.5-km wind vectors (m s^{-1}) for (g) 0800, (h) 1000, and (i) 1200 UTC 6 Oct 2014. The edge of the strong capping inversion at 1200 UTC is shown by the dashed red line in (i). All surface values correspond to the lowest model level. Radar reflectivity is taken at 500 m AGL.
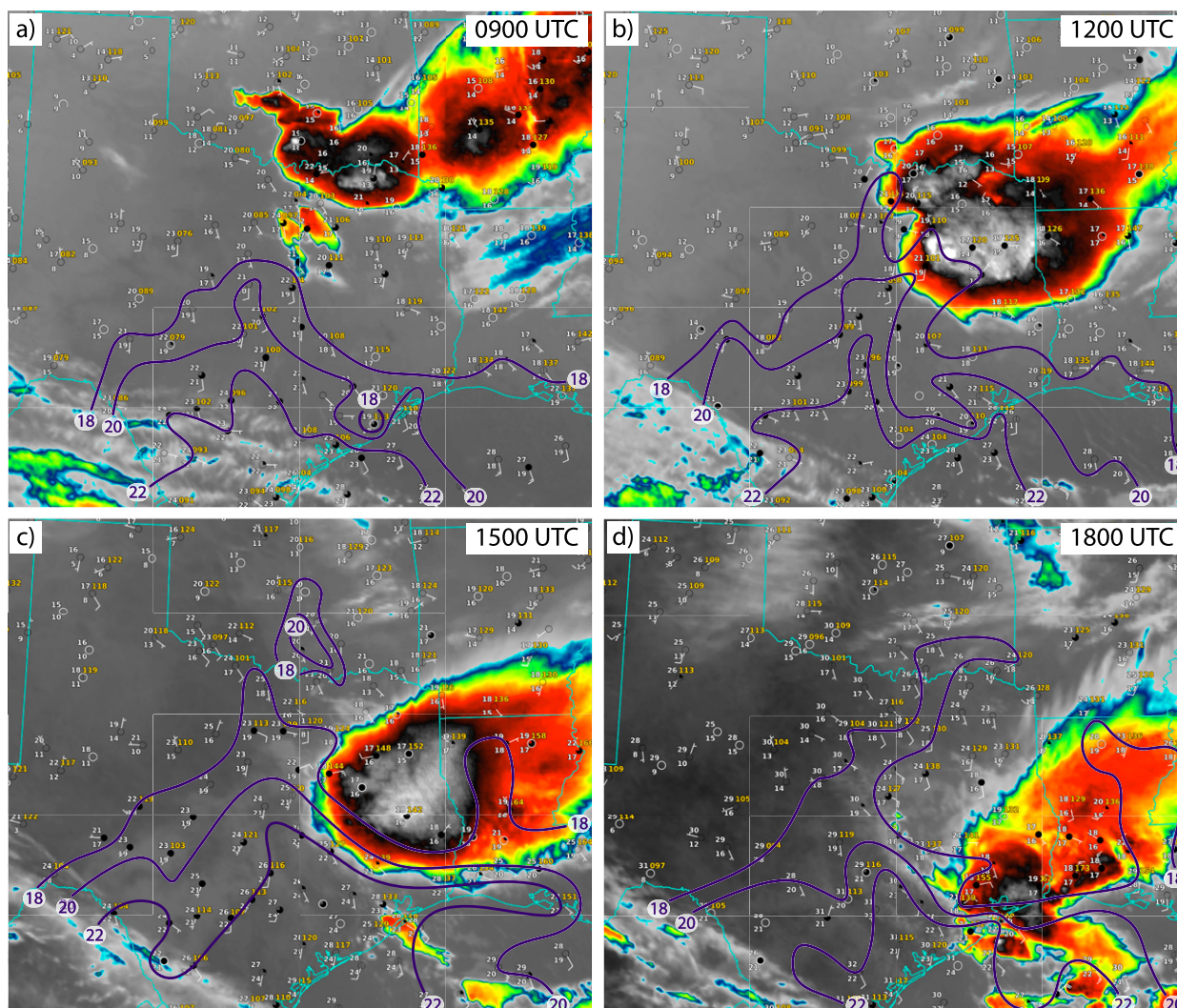
FIG. 12. ASOS observations overlaid with *GOES-13* 10.7-μm IR satellite imagery at (a) 0900, (b) 1200, (c) 1500, and (d) 1800 UTC 6 Oct 2014. Dewpoint temperatures of 18°, 20°, and 22°C are contoured in violet.

the eastern edge of the Balcones Escarpment (Figs. 11a–f). Additionally, the intensification of the surface low during the night further promoted the northward advancement of the moisture plume along the sloping terrain. The passage of the plume boundary led to the erosion of the nocturnal inversion, rise in the LLJ height (Figs. 10b,c), increase in low-level moisture (Figs. 10e,f), and resultant increase in both elevated and surface-based CAPE (Figs. 10h,i). To our knowledge, no prior studies have examined the influence that such prominent moisture plumes have on nocturnal convection within central Texas.

The effects of baroclinicity on the LLJ structure are more pronounced within regions of strongly sloped terrain, which were spatially varying owing to the complex topography of west Texas. Using the inference that spatial gradients in buoyancy generate horizontal vorticity,

Gebauer et al. (2018) explained that the most pronounced westerly flow component would develop near the top of the LLJ in the presence of terrain that increases most predominantly in elevation toward the west. Therefore, the Balcones Escarpment was highly conducive to the development of a height-veering LLJ, which augmented the flow around the surface low located to the north of this region. As a result, high-θ air that originated within the residual layer over the Edwards Plateau was advected over the northward-advancing moisture plume and region of lower terrain by southwesterly flow located near the top of the LLJ (Figs. 11g–i). This persistent differential advection promoted the development of a pronounced capping inversion (Fig. 10), which moved progressively farther eastward throughout the night as the LLJ veered with time. The propensity for capping

inversion development in response to differential advection by the LLJ in the presence of sloping terrain was discussed by Fedorovich et al. (2017) and Gebauer et al. (2018).

As a consequence of differential advection, the narrow corridor of high CAPE located adjacent to Balcones Escarpment was associated with CIN $\approx$ 100–200 J kg^{-1} throughout much of the night (not shown), precluding the development of convection within this region. However, the temporal veering of the LLJ and evolution of the surface low eventually caused the moisture plume to advance northeastward away from the Balcones Escarpment (Figs. 11c, 12b), which resulted in "lid underrunning" (e.g., Carlson et al. 1983) and thus provided the southwestern portion of the simulated MCS with a weakly capped source of conditionally unstable air by 1200 UTC (Figs. 11f,i). The impacts of such differential advection and mesoscale heterogeneity on the structure and evolution of the MCS are now detailed in the following section.

6. Influence of mesoscale heterogeneity on convective evolution and dynamics

a. Formation of RIJ and bow echo

As was previously discussed, QLCS-W reorganized into a bow echo near the Oklahoma-–Texas border. In the WRF simulation, this reorganization occurred after 0800 UTC as the convection moved to the south of the erroneous outflow boundary and into an environment that was undisturbed by the previous convection. The simulated convection subsequently intensified as it encountered a mesoscale corridor of high CAPE supported by the temporally veering LLJ, and a pronounced surface cold pool and bow echo structure had developed by 1000 UTC (Fig. 13). At 1000 UTC, an elevated layer with CAPE $\approx$ 1000–2250 J kg^{-1} and CIN $<$ 50 J kg^{-1} was located immediately ahead of the bow echo, and parcels originating within this layer required $\Delta z_{LFC} \approx$ 1.2–1.5 km (Figs. 13b,c). Furthermore, the near-surface layer was characterized by CAPE $\approx$ 500–750 J kg^{-1}, which required $\Delta z_{LFC} \approx$ 3 km in order to be realized. At this time, pronounced horizontal convergence (as was inferred from the system-relative winds) was collocated with the leading edge of the cold pool and extended throughout the lowest ~5 km. Such implied forced ascent was more than sufficient to lift air residing in both the high-CAPE and near-surface layers to its LFC, which suggests that the bow echo might have become surface-based. Regardless, the apparent capability of the cold pool to lift a deep layer of conditionally

unstable air to its LFC was likely of utmost importance in promoting the continued invigoration of the system.

As the convection intensified and the cold pool strengthened, the system acquired a pronounced upshear-tilted structure (where "upshear" is defined relative to an environmental layer with the LLJ located at its base; Fig. 14). Using a horizontal vorticity balance framework to explain the "optimal state" for continued regeneration of convection within an MCS, Rotunno et al. (1988) (hereafter RKW theory) described the acquisition of an upshear tilt for newly developing cells along an outflow boundary as the consequence of horizontal vorticity generated baroclinically across the outflow boundary becoming dominant over the horizontal vorticity associated with the low-level vertical wind shear. RKW theory was established using a 2D, steady-state, horizontally homogeneous environment with a well-mixed PBL and a unidirectional shear profile, which may limit its applicability in environments that have a near-surface inversion, nocturnal LLJ, and/or considerable horizontal heterogeneity (French and Parker 2010; Coniglio et al. 2012). Additionally, this vorticity balance framework becomes complicated by the acquisition of an upshear tilt, which may promote the development of an RIJ. Weisman (1992) expanded RKW theory to account for the development of an RIJ and its effect on MCS structure by considering the role of horizontal buoyancy gradients ($\partial B/\partial x$) induced by convection.

Weisman (1993) later applied this expanded framework to describe how the interaction between the RIJ and bookend vortices may lead to the genesis of a bow echo. In the presence of a strong cold pool, bookend vortices along a finite line owe their existence to the vertical tilting and subsequent stretching of horizontal vorticity generated baroclinically across the outflow boundary (Weisman and Davis 1998; Wakimoto et al. 2015). These counter-rotating vortices may promote RIJ intensification and bow echo development by focusing the RIJ into a narrow corridor oriented toward the front of the convective line (Weisman 1993; Wakimoto et al. 2015). Additionally, bow echo formation has been attributed to enhanced latent cooling and downward momentum transport arising from the development of an RIJ (e.g., Mahoney et al. 2009; Mahoney and Lackmann 2011).

At 1000 UTC, an RIJ was evident within the trailing-stratiform region and remained largely elevated until impinging upon the rear of the convective line and abruptly descending within convective downdrafts (Fig. 14). Consistent with the Weisman (1992) framework, the RIJ was located along and beneath a region characterized by
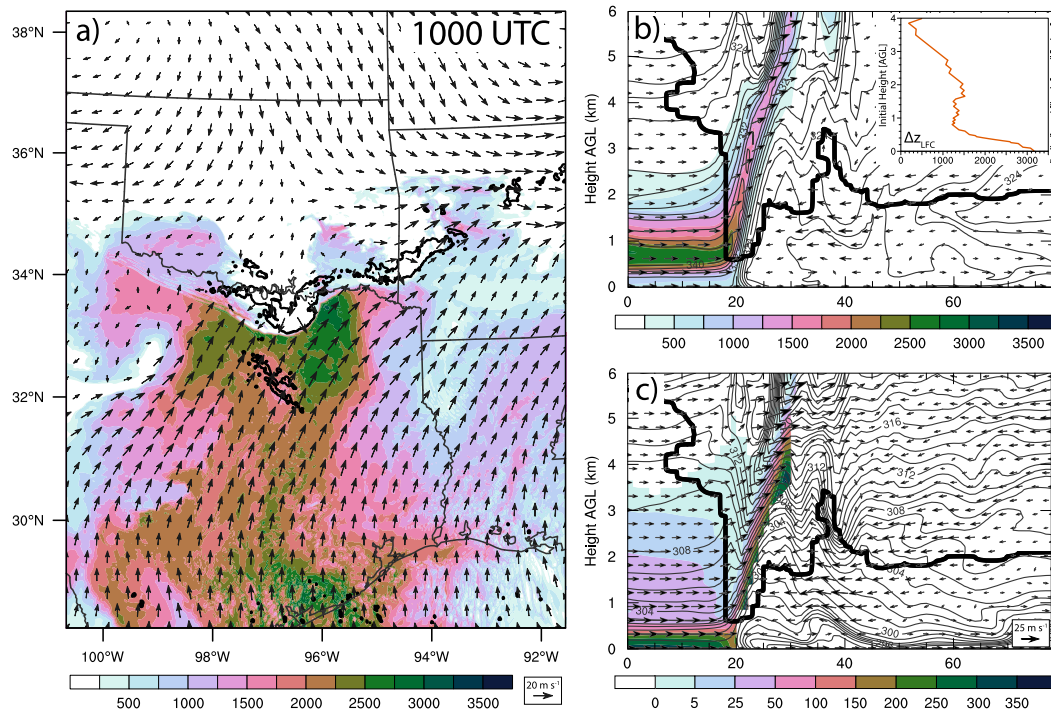
FIG. 13. WRF depiction of (a) CAPE (shaded; J kg^{-1}), 0-dBZ radar reflectivity (contours), and horizontal winds (vectors; m s^{-1}) for parcels originating at 500 m AGL at 1000 UTC 6 Oct 2014. Vertical cross sections of (b) CAPE (shaded; J kg^{-1}) and θ_e (contours; K), and (c) CIN (shaded; J kg^{-1}) and θ_v (contours; K) taken through the leading edge of the bow echo are also shown at 1000 UTC. System-relative wind vectors (m s^{-1}; system motion is from right to left in this and other figures herein) and the cloud boundary (cloud water mixing ratio + cloud ice mixing ratio + snow mixing ratio = 0.0001 g kg^{-1}; thick black contour) are depicted in both panels. The vertical profile of Δz_{LFC} in (b) is valid at $x = 0$ km. The cross sections were zoomed in on the path depicted in Fig. 14.

$\partial B/\partial x < 0$, which yielded horizontal vorticity oriented such that rear-to-front system-relative flow was induced beneath the trailing anvil. This induced flow had originated at mid- to upper levels within a region of RH < 20% (Fig. 14b), which appeared to result from both subsynoptic-scale subsidence that developed behind the upper-level short-wave trough (Fig. 15) and mesoscale subsidence induced by the MCS itself (Fig. 14c; e.g., Nicholls et al. 1991; Adams-Selin and Johnson 2013).

The importation of this dry air into the system likely enhanced latent cooling via evaporation and sublimation and thus strengthened the cold pool circulation. Additionally, bookend vortices were located on either side of the convective line (Fig. 16), and the strongest rear-to-front flow was laterally confined to a narrow corridor located between them. Therefore, the bookend vortices presumably augmented the RIJ and focused it toward the front of the system. As the RIJ approached the rear of the convective line and abruptly descended, strong north-northwesterly momentum was transported downward toward the surface, which enabled the bow echo to accelerate toward the south-southeast in deviation from the motion of the upper-level disturbance. The

convection was thenceforth maintained primarily via convective dynamics and moisture convergence provided by the LLJ.

b. Evolution of bore and backbuilding convection

As the primary convective line was reorganizing into a bow echo, a long-lived wave train was developing simultaneously to its west over southwestern Oklahoma (Figs. 17a,b). This wave train continued to move in tandem with the MCS until sunrise, at which point PBL mixing led to the erosion of the wave duct.

An internal bore is a type of gravity wave disturbance that may be generated by the intrusion of a density current into a near-surface stable layer (Rottman and Simpson 1989). Bore passages are characterized by a hydraulic jump and thus typically result in the sustained upward displacement of the low-level inversion. However, bores may evolve over time into an amplitude-ordered train of solitary waves, or a soliton (Christie 1989; Knupp 2006; Koch et al. 2008a; Toms et al. 2017). Bores and solitons can persist for several hours if conditions are sufficient for the trapping of vertically propagating wave energy within a wave duct (e.g., Scorer 1949; Lindzen and
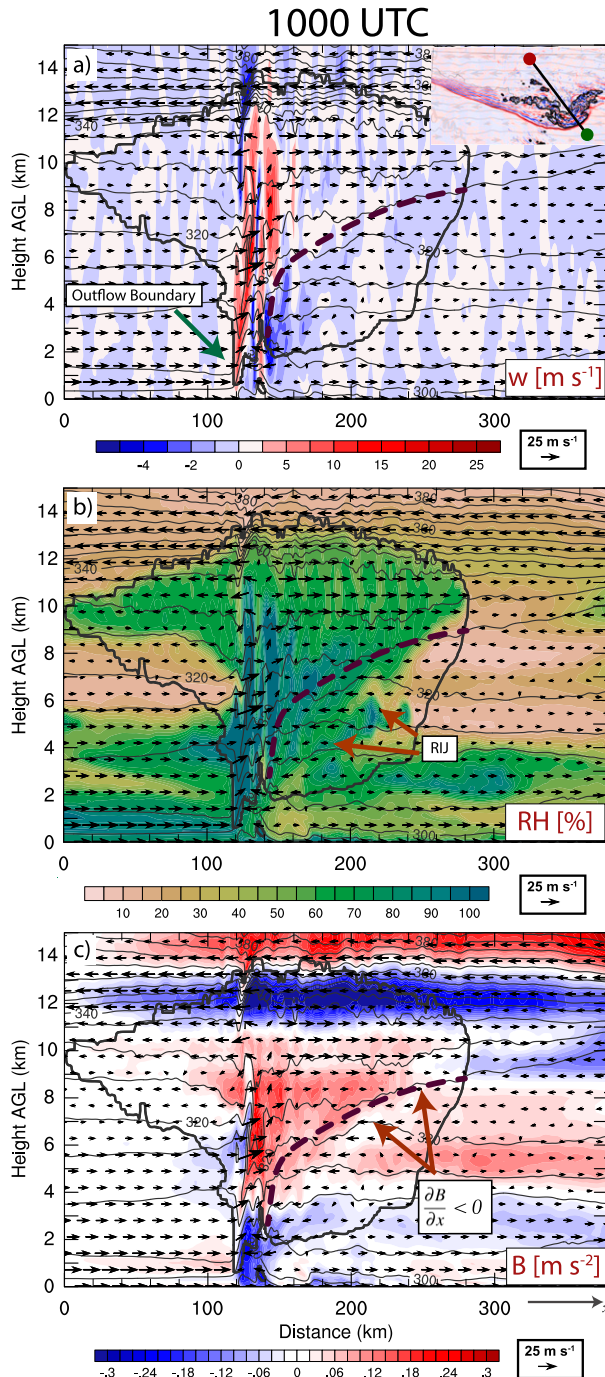
FIG. 14. Vertical cross sections through the bow echo of (a) vertical velocity (shaded; m s^{-1}), (b) relative humidity (shaded; %), and (c) buoyancy (m s^{-2}) for 1000 UTC. System-relative wind vectors (m s^{-1}), θ_v (contours; K), and the cloud boundary (thick black contour) are shown in all panels. The dashed violet line demarcates the separation between the ascending front-to-rear and descending rear-to-front flow branches. The cross-sectional path is displayed in the top panel, where 0 km on the x axis corresponds to the green circle. The buoyancy gradient in (c) assumes that x increases toward the right.

Tung 1976; Crook 1988; Parsons et al. 2019). Oftentimes, the LLJ acts as the wave trapping mechanism within the nocturnal convective environment because it yields a vertical wind profile characterized by pronounced curvature (Crook 1988; Koch and Clark 1999; Koch et al. 2008b; Haghi et al. 2017); such a trapping effect is maximized for waves propagating opposite to the direction of the LLJ (e.g., Koch et al. 1991).

Favorable conditions for wave trapping can be determined by computing the vertical profile of the square of the Scorer parameter ℓ, which is equivalent to the square of the vertical wavenumber m under conditions for which the square of the horizontal wavenumber k is negligible (Scorer 1949). Solutions for wave trapping exist when a layer characterized by $\ell^2 > 0$ is located beneath a layer characterized by $\ell^2 < 0$; the wave duct is therefore the layer in which $\ell^2 > 0$, which satisfies the Taylor–Goldstein equation for wave propagation. The equation for ℓ^2 is given by

$$\ell^2 = \frac{N^2}{(U - C_b)^2} - \frac{\frac{\partial^2 U}{\partial z^2}}{(U - C_b)}, \qquad (2)$$

where N^2 is the square of the Brunt–Väisälä frequency, given by $N^2 = (g/\theta_v)(\partial \theta_v/\partial z)$, θ_v is the virtual potential temperature, C_b is the bore speed, U is the environmental wind component orthogonal to the bore, and $\partial^2 U/\partial z^2$ represents the curvature of the environmental wind profile. The first and second terms on the rhs are the stability and curvature terms, respectively. The average speed that the leading wave moved over a 1-h period was used for C_b.

The far western portion of the wave train was not associated with CI owing to the presence of a deep, dry residual layer over southwestern Oklahoma and the Texas Panhandle and the relatively small amplitudes associated with the waves in this region (Figs. 17a,b). This portion of the wave train exhibited a structure characteristic of a soliton and persisted until sunrise (not shown). However, backbuilding convection developed atop the wave train immediately to the west and in the wake of the bow echo and its associated convective outflow. The wave structure within this region resembled that of an undular bore, wherein each individual wave passage promoted a net upward displacement of the inversion layer (Figs. 17c,d). The evolution of the undular bore and its role in promoting CI is the focus of the following discussion.

The bore developed and propagated within a 400–500-m-deep inversion (Fig. 17c) that had formed in response to radiative cooling within an environment characterized by a deep, residual mixed layer. At 0900 UTC, a
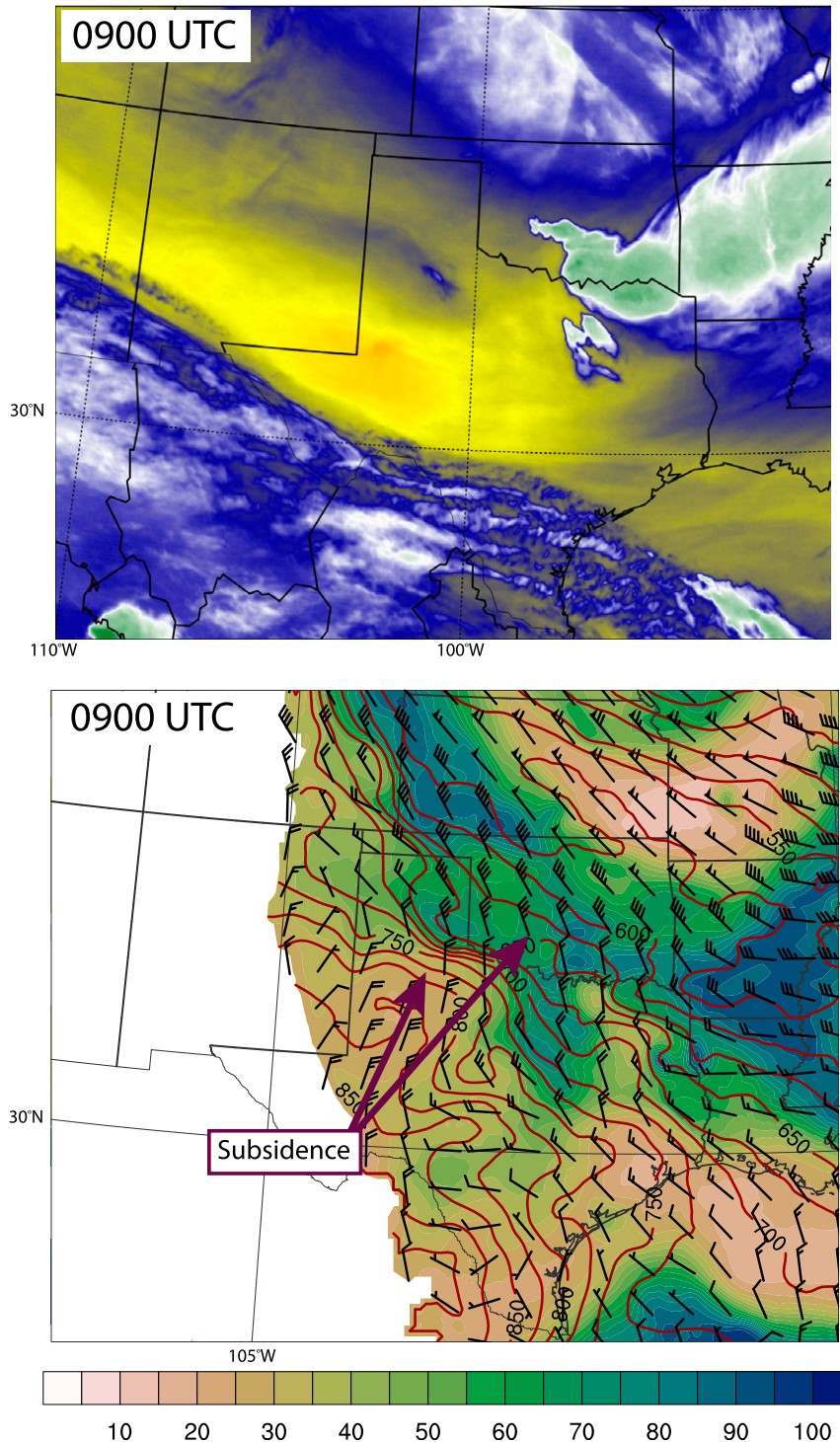
FIG. 15. Depiction of subsidence in the Texas Panhandle region from (top) *GOES-13* 6.7-μm midlevel water vapor imagery at 0615 UTC 6 Oct 2014 and (bottom) relative humidity (shaded; %), isobars (contours; hPa), and flow relative to the motion of the surface low (barbs; kt) on the 309-K isentropic surface from the RAP analysis at 0900 UTC 6 Oct 2014. Warmer colors in the water vapor imagery depict greater infrared brightness temperatures, indicative of lower water vapor concentrations. RAP data below ground have been removed.
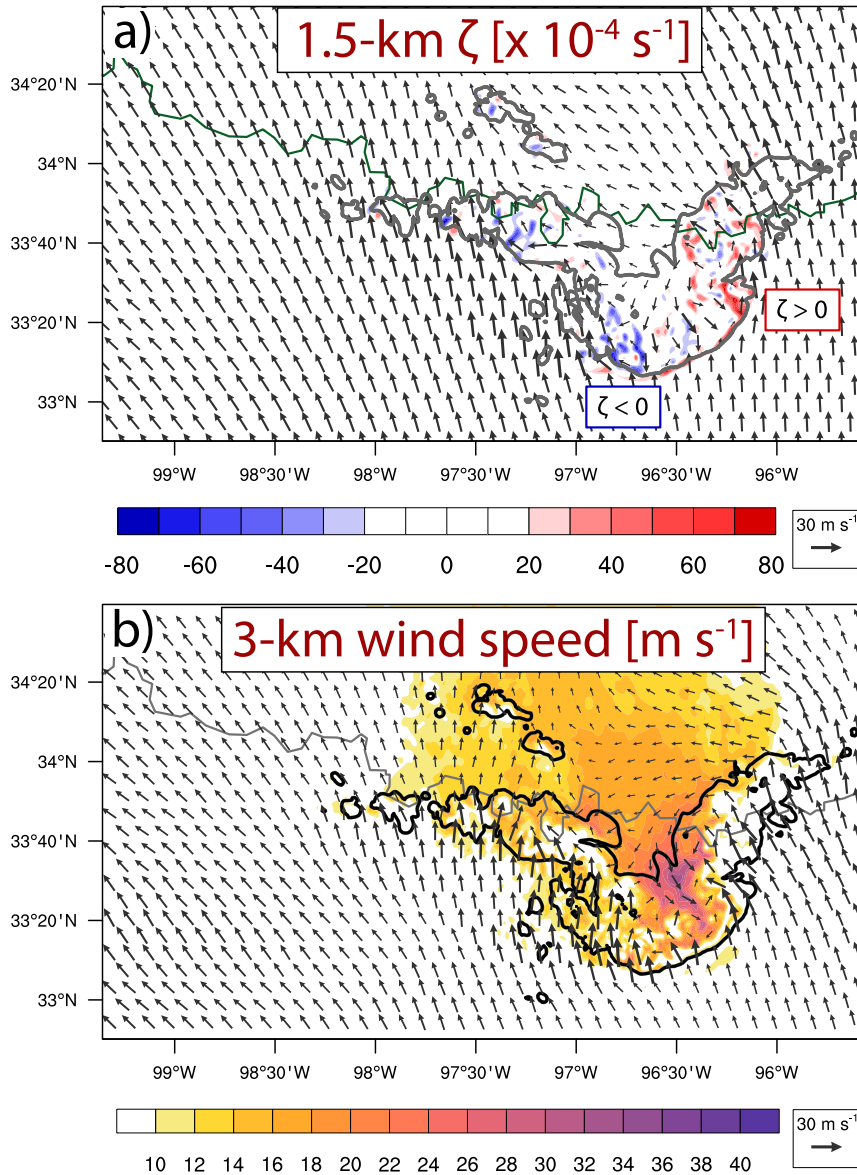
FIG. 16. WRF depiction of (a) 1.5-km vertical vorticity (shaded; $\times 10^{-4}\,\text{s}^{-1}$), 0-dB$Z$ radar reflectivity (contours), and 1.5-km system-relative flow (vectors; m s^{-1}), and (b) 3-km horizontal wind speed (shaded; m s^{-1}), 0-dBZ radar reflectivity (contours), and 3-km system-relative flow (vectors; m s^{-1}) at 1000 UTC 6 Oct 2014. Radar reflectivity is taken at 1 km AGL.

strong, orthogonal LLJ with substantial curvature existed within the environment ahead of the bore (Fig. 18a). The corresponding vertical profile of ℓ^2 was characterized by a transition from strongly positive to negative values at approximately 450 m AGL (Fig. 18c). This transition was almost entirely dominated by a change in sign of the curvature term at this level, which was associated with an inflection point in the wind profile just above the level of maximum winds in the opposing LLJ. Thus, the dominant wave duct was confined

to the lowest 450 m owing to this inflection point, which is consistent with the findings of previous studies (Koch and Clark 1999; Koch et al. 2008b; Haghi et al. 2017; Toms et al. 2017). However, evanescent waves were apparent throughout the lowest ~3 km of Fig. 17c, above which vertically propagating waves were evident beneath ~4.5 km. Therefore, the ducting layer within the lowest 450 m was evidently too shallow to effectively trap wave energy for a vertical wavelength of ~3 km, which is consistent with the expectations from linear
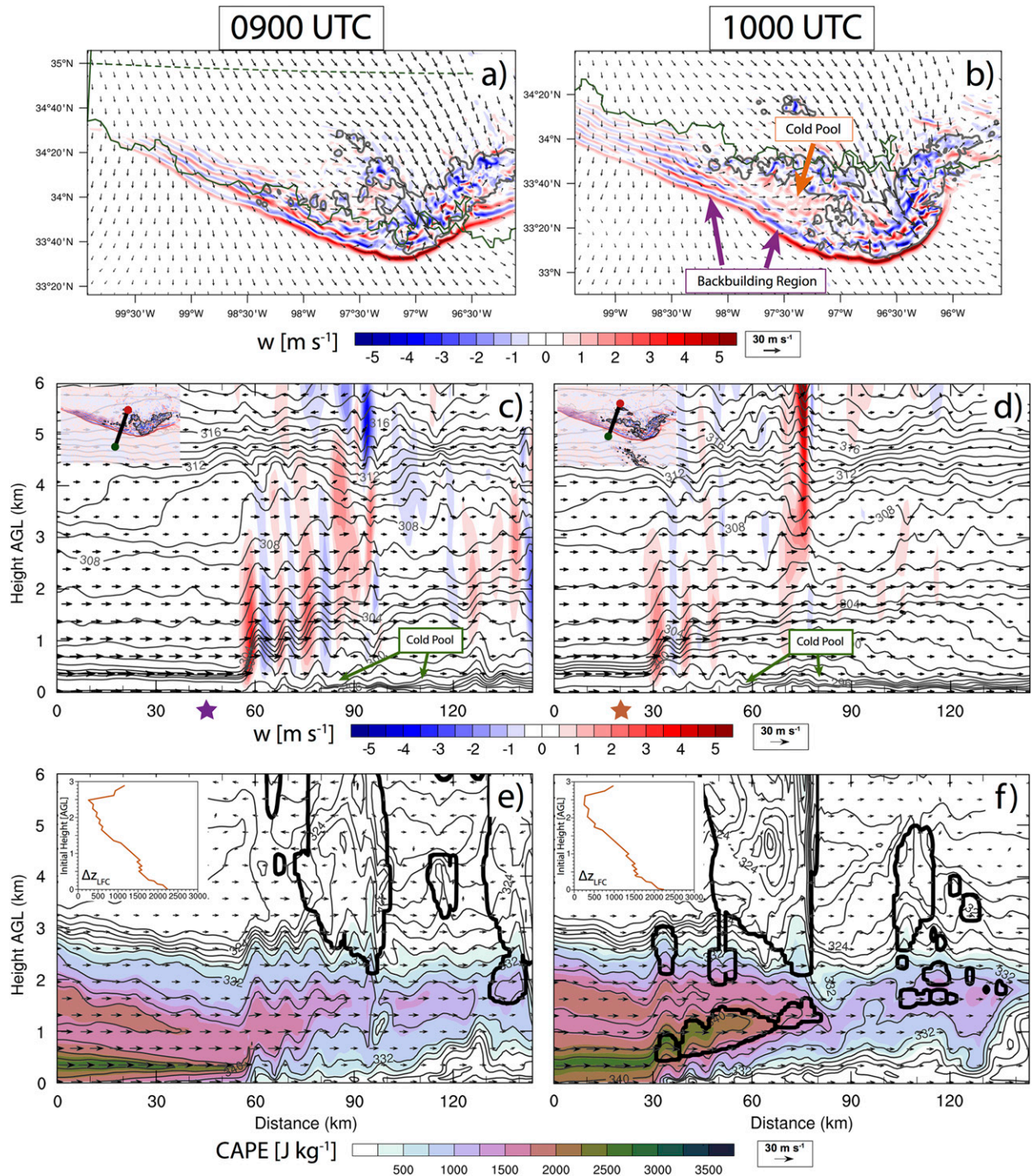
FIG. 17. As in Fig. 16, but for 1-km vertical velocity (shaded; m s^{-1}), 0-dBZ radar reflectivity (contours), and 3-km ground-relative winds (vectors; m s^{-1}) at (a) 0900 and (b) 1000 UTC. Vertical cross sections of (middle) vertical velocity (shaded; m s^{-1}), θ (gray contours; K), and system-relative winds (vectors; m s^{-1}), and (bottom) CAPE (shaded; J kg^{-1}), θ_e (gray contours; K), system-relative winds (vectors; m s^{-1}), and cloud boundary (thick black contour) are shown in (c),(e) at 0900 and (d),(f) at 1000 UTC, respectively. The inflow profiles of Δz_{LFC} depicted in (e) and (f) were computed at the violet and orange stars in (c) and (d), respectively. The cross-section paths are shown in (c) and (d) for each corresponding time.
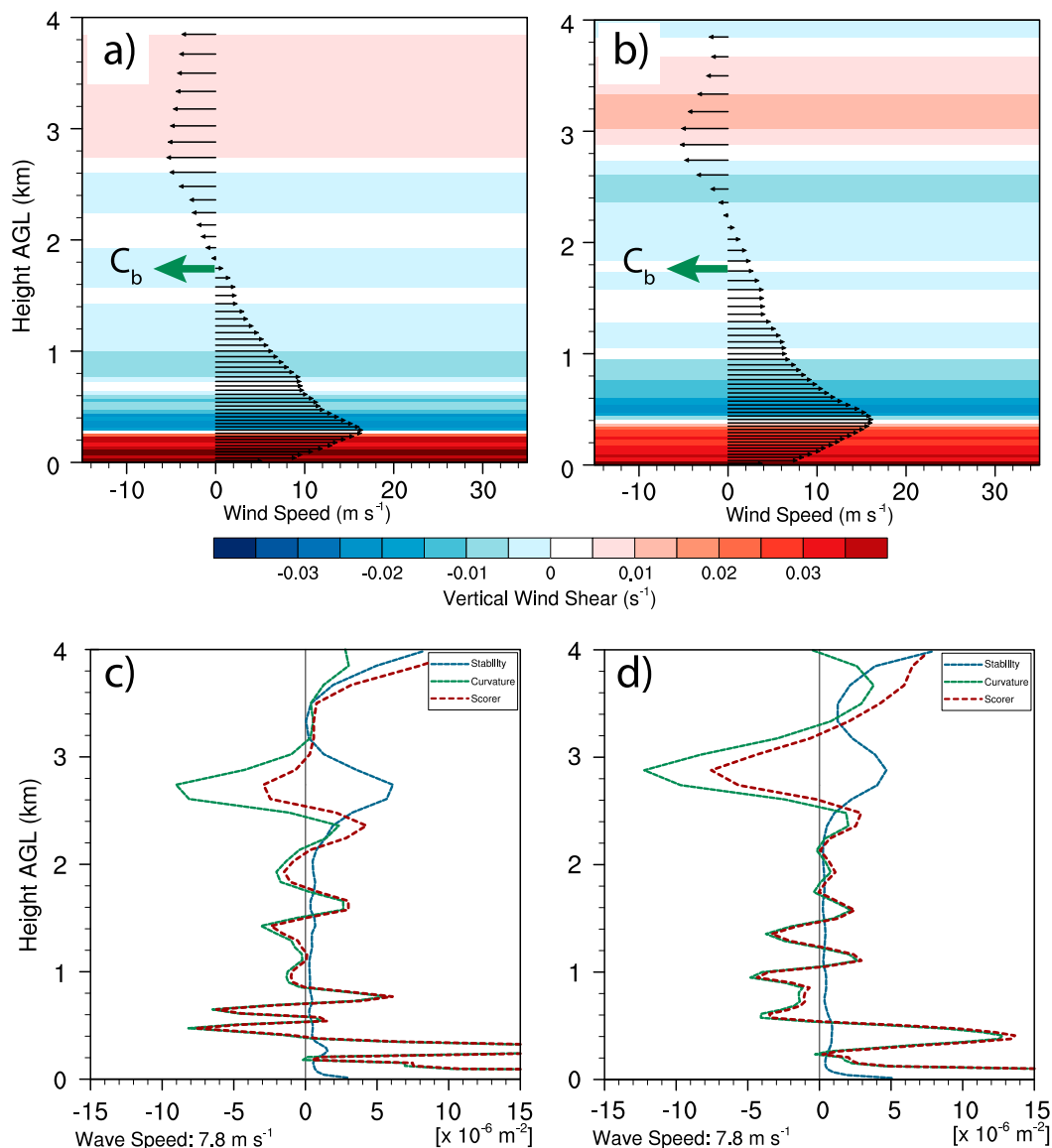
FIG. 18. Inflow profiles ahead of the region of backbuilding convection of (top) wave-orthogonal ground-relative winds (vectors; m s^{-1}) and vertical wind shear (shaded; s^{-1}) for (a) 0900 and (b) 1000 UTC and (bottom) Scorer parameter for (c) 0900 and (d) 1000 UTC. The profiles for 0900 and 1000 UTC were computed at the violet and orange stars in Fig. 17, respectively.

wave theory (Lindzen and Tung 1976). Additionally, the inflow wind profile lacked any discernible critical level (Fig. 18a), although a reversal in the system-relative winds was apparent at ~4.25 km directly above the waves (Fig. 17c). Because this critical level was located within a layer of high static stability, it was unlikely to have aided in wave trapping (Booker and Bretherton 1967).

By 1000 UTC, the amplitudes of the trailing waves had decreased significantly, although the leading bore was still quite pronounced (Fig. 17d). Between 0900 and 1000 UTC, the moisture plume had advanced

northwestward around the low and become located adjacent to this portion of the bore (Figs. 11b,e). The modifications to the vertical wind and stability profiles arising from the passage of the moisture plume further reduced the effectiveness of the low-level wave duct (Figs. 18b,d). Additionally, no distinct critical level was apparent within the environment at this time. Figures 17a,b indicate that the 3-km wind field had been significantly altered by the bow echo, which resulted in winds that were oriented approximately parallel to the bore within this region. Therefore, the further degradation of

the low-level wave duct and the midlevel flow modifications induced by the bow echo likely caused this portion of the bore to weaken considerably between 0900 and 1000 UTC. In contrast, the 3-km wind field in proximity to the long-lived soliton was less prominently affected by the bow echo, which may have increased the likelihood that a critical level contributed to wave trapping within this region.

Backbuilding convection had formed atop the bore by 0900 UTC and became more widespread with time (Figs. 17a,b). Along the path shown in Figs. 17c–f, convection first developed ~25 km behind the leading wave at 0900 UTC as elevated air originating primarily between ~1 and 2.5 km AGL was progressively lifted until it reached its LFC. Although the highest CAPE was located within the lowest ~700 m, air within this layer required $\Delta z_{LFC} > 1.5$ km and was therefore unlikely to have reached its LFC after traversing just 25 km. However, a layer of high-θ_e air extended rearward from the updraft located at $x \approx 90$ km, which continued to gradually ascend over the cold pool. A second convective cell was located at $x \approx 140$ km, which likely formed once air within the high-θ_e layer was eventually lifted to its LFC. Despite that the bore had weakened by 1000 UTC, the cold pool within this region had deepened such that CI was still supported (Figs. 17b,d). Net upward displacements of a few hundred meters occurred as environmental air was lifted over the bore and trailing cold pool, which was adequate for air originating between ~1.5–2.5 km to reach its LFC (Figs. 17d,f). Therefore, the expanding convective cold pool enabled backbuilding CI to continue once the bore could no longer provide sufficient lifting. Over time, the backbuilding convection and bow echo congealed, which helped to promote the evolution into an organized LLTS MCS.

The evolution of the backbuilding convection exhibited some similarity to the conceptual model provided by Peters and Schumacher (2015), who showed that sustained ascent of capped, but conditionally unstable air over a cold pool can promote backbuilding CI. In their study, the outflow boundary was unable to initiate convection owing to both the existence of low-level CIN and the presence of a strong LLJ oriented orthogonal to the boundary, which yielded horizontal vorticity of the same orientation as that produced baroclinically across the outflow boundary. However, because the backbuilding convection herein initially formed as elevated air was lifted by a bore, the presence of a strong, orthogonal LLJ was necessary because it helped to provide the duct required to maintain the waves. Additionally, the magnitude of the cold-pool-relative winds, which is modulated by the LLJ, is one factor within hydraulic theory that determines whether or not a bore will develop ahead of a density current (Rottman and Simpson 1989; Koch

et al. 1991; Haghi et al. 2017). Therefore, the role that the low-level wind profile has in the development of backbuilding convection varies based upon the phenomenon responsible for lifting air to its LFC. Similar findings were noted by French and Parker (2010), who described how the orientation and magnitude of the low-level shear affected RKW balance for a cold-pool-driven system, but as the system became bore driven, the low-level shear modulated the amplitude of the bore.

c. Evolution into leading-line, trailing-stratiform MCS

After the reorganization of QLCS-W into a bow echo with a trailing region of backbuilding convection, the system continued toward the south-southeast and ultimately merged with a convective cluster that had developed over north-central Texas at approximately 0900 UTC (Figs. 1c, 12a). By 1000 UTC, this cluster had formed within the WRF simulation in nearly the same location as the observed convection (Fig. 13a). The simulated convective cluster, which developed just to the north of $x = 300–350$ km in Fig. 10, was sustained by elevated CAPE that had materialized as a result of differential moisture advection by the temporally and height-veering LLJ. The convective cluster formed near the collocation of the leading edge of the moisture plume (Figs. 10f, 11b) and an eastward-moving band of elevated convergence (Fig. 10c), which was located downstream from the Edwards Plateau and region of strongest capping (Fig. 11h). Therefore, the processes that likely led to CI were largely consistent with the recent findings of Gebauer et al. (2018), who described how mesoscale heterogeneity in LLJ structure produces elevated convergence and differential moisture advection, which can promote nocturnal CI in the absence of a surface boundary.

This convective cluster merged with the western portion of the observed bow echo after 1200 UTC (Fig. 1d), whereas the cluster merged with the southeastern flank of the simulated bow echo (Fig. 8d). As a result, the western portion of the observed MCS intensified following the merger, while the eastern portion of the simulated MCS intensified. Because the cluster formed in nearly the same location in both the observations and WRF simulation, this discrepancy was likely attributed to the aforementioned westward bias in the location of the simulated bow echo. Regardless of this difference, both the observed and simulated MCSs acquired a LLTS structure after 1200 UTC.

The southwestern flank of the MCS was located adjacent to the moisture plume in both the observations and WRF simulation by 1200 UTC (Figs. 11c, 12b).

The simulated moisture plume had underrun the northeastern extent of the strong capping inversion by this time (Fig. 11i), and thus a minimally capped corridor of high surface-based CAPE ($>1500\,\mathrm{J\,kg^{-1}}$; Fig. 11f) was located beside the outflow boundary prior to sunrise. At 1300 UTC, which was shortly after sunrise but prior to any appreciable insolation (Fig. 19a), the inflow region lacked a near-surface inversion, and CAPE $> 1750\,\mathrm{J\,kg^{-1}}$ existed over the lowest $\sim1\,\mathrm{km}$ (Figs. 19g, 20a). Surface parcels required $\Delta z_{\mathrm{LFC}} \approx 2\,\mathrm{km}$, which steadily decreased to $\Delta z_{\mathrm{LFC}} \approx 1.1\,\mathrm{km}$ for parcels originating at $1\,\mathrm{km}$ AGL (not shown). A deep surface cold pool had developed by this time, which presumably provided sufficient lifting for both elevated and near-surface parcels to reach their LFCs as they were swept rearward behind the outflow boundary. Therefore, the existence of a deep cold pool supported the potential for the southwestern portion of the MCS to become surface based prior to sunrise as it interacted with the low-level moisture plume. Strong southwesterly inflow provided sustained low-level moisture convergence along this flank of the system, which supported its invigoration and helped to augment the developing trailing-stratiform region (Fig. 8d).

d. Response to solar heating

Prior to the onset of solar heating, the θ_v differential across the cold pool was largest along the southwestern flank of the MCS owing to the presence of the low-level moisture plume (Fig. 19d). In addition to its characteristically high water vapor concentration, widespread low-level cloud cover existed within the plume (Fig. 12b). The net radiation (R_{NET}), which is defined as

$$R_{\mathrm{NET}} = (1 - \alpha)R_{\mathrm{SW}\downarrow} + R_{\mathrm{LW}\downarrow} - \varepsilon\sigma T_{\mathrm{SFC}}^4, \qquad (3)$$

where α is the surface albedo, $R_{\mathrm{SW}\downarrow}$ is the net downwelling shortwave radiation, $R_{\mathrm{LW}\downarrow}$ is the net downwelling longwave radiation, ε is the surface emissivity, σ is the Stefan–Boltzmann constant, and T_{SFC} is the ground surface temperature, depicts that the enhanced moisture and low-level cloud cover contributed a net surface heating effect throughout the plume during the nighttime (Fig. 19a). As a result, contributions from both radiation and advection supported the high values of surface θ_v within this region.

By 1500 UTC, solar radiation had increased surface temperatures across southeastern Texas, and the low-level cloud cover within the moisture plume was still evident to the southwest of the MCS (Fig. 12c). The net radiation R_{NET} had increased considerably throughout the WRF domain in association with the onset of insolation by this time (Fig. 19b), and the effects of low-level cloud cover on

the radiation and θ_v fields remained apparent within the plume, although the cloud cover instead acted to reduce the surface heating within this region (Fig. 19e). To the south of the MCS, where clouds were either absent or sporadic, the onset of insolation promoted considerable and rapid increases in both θ_v and surface-based CAPE (Fig. 19h). Such an abrupt increase in surface-based CAPE was attributed to both surface warming and the downward transport of elevated moisture that had been advected inland from over the Gulf of Mexico by the LLJ.

Overall, the MCS had become better organized by 1500 UTC, but the system had acquired a highly asymmetric shape as convection along the western and southwestern flanks had weakened (Figs. 1e, 8e). Consequently, the western portion of the trailing-stratiform region had begun to erode, and the strongest convection was located along the southern and southeastern flanks of the MCS (Fig. 12c). Despite the presence of cloud cover ahead of the southwestern flank, the cold pool within this region had become shallower with time (cf. Figs. 20a,b) as the θ_v gradient across the outflow boundary increased in response to differential heating. Moreover, this flank of the MCS had moved into the strongly capped environment to the east of the Edwards Plateau, and the high-CAPE air located beneath $\sim1\,\mathrm{km}$ required $\Delta z_{\mathrm{LFC}} \approx 1.3\text{–}2.1\,\mathrm{km}$. Therefore, the weakening convection along the southwestern flank was highly elevated and developed only after this air had been swept sufficiently rearward over the cold pool. In contrast, the capping inversion was weaker in southeastern Texas, and thus the southern portion of the MCS remained intense as a deep cold pool sufficiently lifted air with CAPE $> 2500\text{–}3000\,\mathrm{J\,kg^{-1}}$ to its LFC (Fig. 20c).

After 1700 UTC, the trailing-stratiform region was almost entirely absent, and the remaining convective line began to interact with clusters moving inland from over the Gulf of Mexico (Figs. 1f, 12d). Continued surface heating had promoted further increases in environmental θ_v to the south of the MCS (Figs. 19c,f), and surface-based CAPE values of $2000\text{–}3000\,\mathrm{J\,kg^{-1}}$ enabled strong convection to continually develop along the outflow boundary (Figs. 19i, 20d). However, outflow and cloud cover associated with inland-moving convection had begun to modify the near-storm environment along the southern and southeastern flanks of the MCS, and mesoscale regions of diminished CAPE developed in the wake of these clusters. As a result of these destructive effects, the remaining convective line became increasingly disorganized with time, but several clusters of strong convection persisted within the weakly capped, conditionally unstable environment as they moved over the Gulf of Mexico during the afternoon (Figs. 1f, 8f).
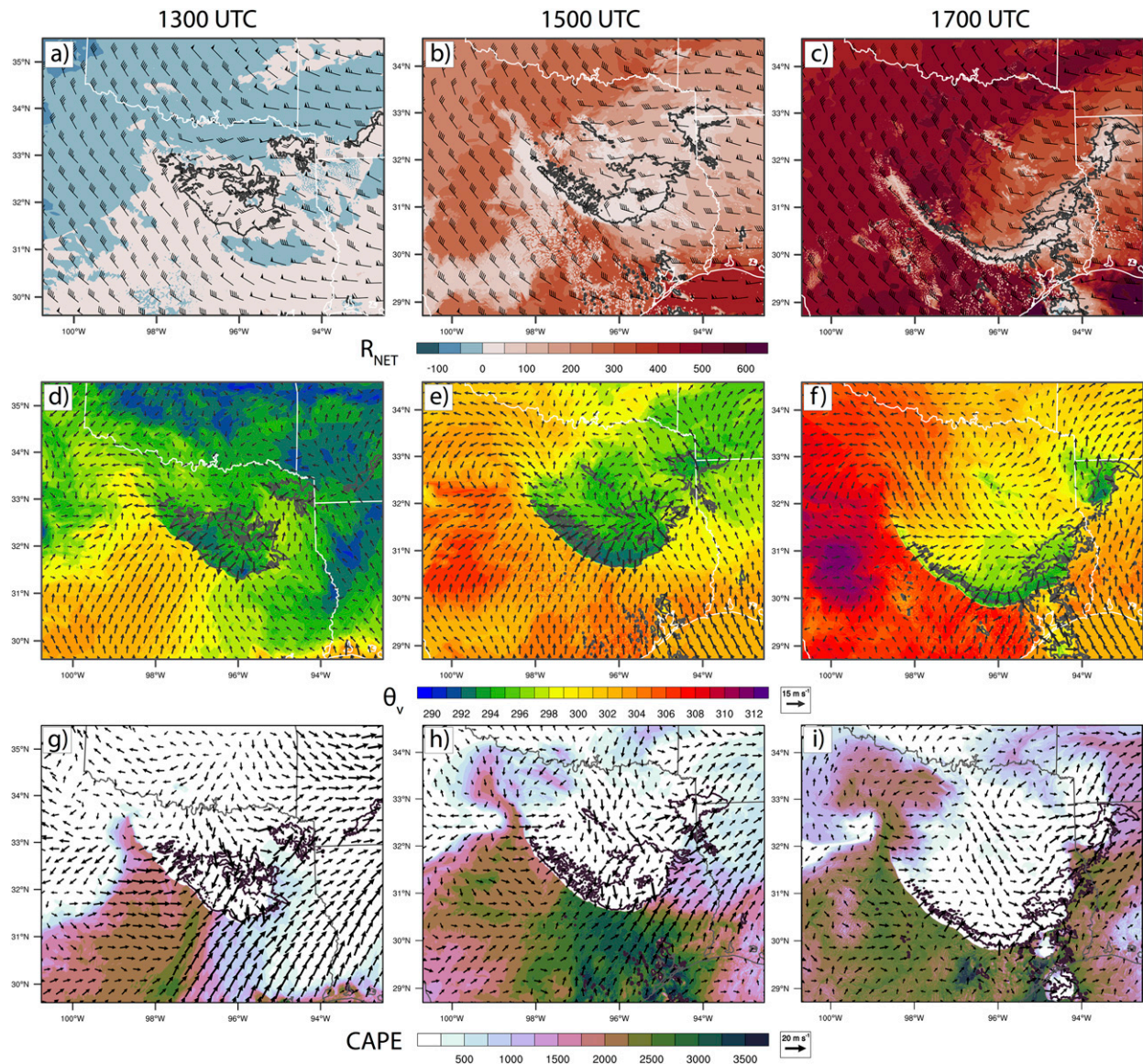
FIG. 19. WRF depiction of net radiation (shaded; $W\,m^{-2}$), 0-dBZ radar reflectivity (gray contour), and 300-hPa horizontal winds (barbs; kts) for (a) 1300, (b) 1500, and (c) 1700 UTC; surface θ_v (shaded; K), 0-dBZ radar reflectivity (black contour), and ground-relative surface winds (vectors; $m\,s^{-1}$) for (d) 1300, (e) 1500, and (f) 1700 UTC; and surface-based CAPE (shaded; $J\,kg^{-1}$), 0-dBZ radar reflectivity (violet contour), and 0–1-km bulk wind difference (vectors; $m\,s^{-1}$) for (g) 1300, (h) 1500, and (i) 1700 UTC 6 Oct 2014. All surface values correspond to the lowest model level. Radar reflectivity is taken at 500 m AGL.

7. Summary and conclusions

This study provided a thorough investigation into the multiscale processes contributing to the development, reorganization, and daytime persistence of a nocturnal MCS on 6 October 2014. This MCS originated from two elevated convective clusters that developed in response to enhanced frontogenesis in the presence of a nocturnal LLJ. These clusters quickly grew upscale into a QLCS, which produced numerous severe reports and a nocturnal tornado within central Oklahoma. The QLCS

subsequently weakened and split into two portions, and QLCS-E continued to move southeastward in tandem with the upper-level disturbance. In contrast, QLCS-W reorganized into a bow echo with a pronounced cold pool and RIJ as it encountered an increasingly unstable environment supported by the LLJ. An undular bore developed immediately to the west of the bow echo, and sustained ascent of warm, moist air over the bore and trailing cold pool led to the development of back-building convection. The bow echo and backbuilding
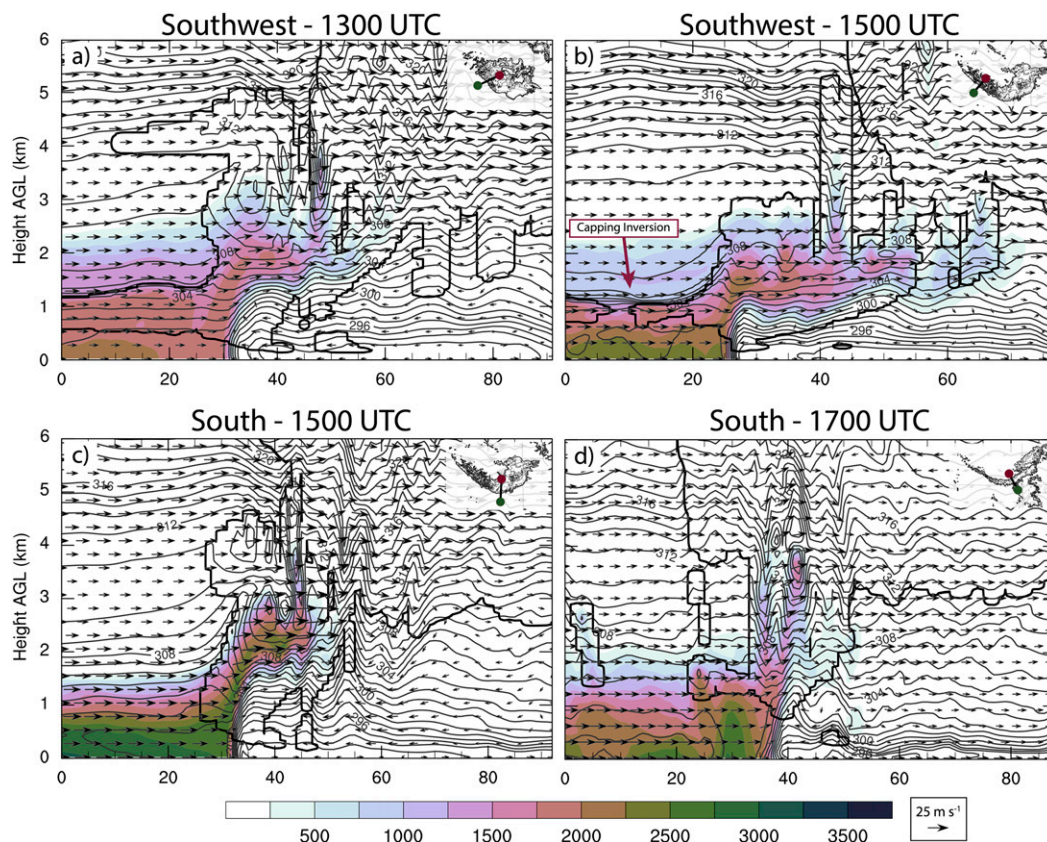
FIG. 20. Vertical cross sections of CAPE (shaded; J kg^{-1}), system-relative wind vectors (m s^{-1}), θ_v (contours; K), and cloud boundary (thick black contour) taken through the southwestern portion of the MCS at (a) 1300 and (b) 1500 UTC and the southern portion of the MCS at (c) 1500 and (d) 1700 UTC 6 Oct 2014. The paths for each cross section are shown in the top-right corner of each respective panel.

convection congealed with time, and the system eventually organized into a LLTS MCS as it moved toward the south-southeast.

The mesoscale environment was characterized by considerable heterogeneity owing to the interaction between the LLJ and the topography of west Texas. Following the onset of the LLJ, a narrow moisture plume characterized by high surface-based CAPE advanced northward parallel to the Balcones Escarpment. Additionally, the development of a spatially heterogeneous LLJ led to the formation of a strong capping inversion to the east of the Edwards Plateau. The northeastern extent of the moisture plume eventually underran the capping inversion and became adjacent to the southwestern flank of the MCS, which supported its invigoration and the development of a strong cold pool. The resultant enhancement of convection along this flank helped to augment the developing trailing-stratiform region and thus aided in the organization of the MCS. Additionally, elevated convergence associated with the spatially heterogeneous LLJ led to the

initiation of a convective cluster over north-central Texas, which ultimately merged with the MCS after 1200 UTC.

Following the commencement of solar heating, surface-based CAPE rapidly increased across southeastern Texas owing to both surface warming and downward moisture transport. As a result, strong convection persisted along the southern and southeastern flanks of the MCS as the strong cold pool sufficiently lifted the destabilizing near-surface air to its LFC. However, convection along the southwestern flank weakened considerably after sunrise as it moved into an increasingly capped environment east of the Edwards Plateau. By 1700 UTC, the stratiform region had completely eroded, and the MCS became progressively disorganized as it subsequently interacted with convection moving inland from over the Gulf of Mexico. Despite these interactions, the presence of an established cold pool and high CAPE permitted strong convective clusters to persist into the afternoon as they moved off the Gulf Coast.

The close proximity of the MCS to the Gulf of Mexico enabled its inflow environment to rapidly destabilize—both during the nighttime and after sunrise—as abundant moisture was readily advected inland by the LLJ. As a result, the cessation of the LLJ did not diminish the source of conditionally unstable air for the MCS, as might have occurred with other nocturnal systems located farther to the north. Instead, the onset of solar heating in the presence of prevailing southerly flow further increased CAPE throughout the inflow region. However, the ability for the MCS to become organized and develop a strong cold pool prior to sunrise was also crucial for its daytime persistence because 1) the maintenance mechanism for a wave-driven system would have dissipated with the onset of daytime PBL mixing, and 2) the presence of a capping inversion over much of the region meant that significant lifting was still required for the rapidly destabilizing low-level air to reach its LFC. Because the topography of Texas had such a strong influence on establishing considerable heterogeneity within the environment, which ultimately had important implications for the evolution and longevity of the MCS, the applicability of these findings to persistent MCSs located outside of this region may be limited. Therefore, additional observational and numerical modeling studies of long-lived MCSs are needed, both within and outside the southern Great Plains, to determine whether or not the processes discussed herein can be more broadly applied to other cases of daytime persistence.

REFERENCES

Adams-Selin, R. D., and R. H. Johnson, 2013: Examination of gravity waves associated with the 13 March 2003 bow echo. *Mon. Wea. Rev.*, **141**, 3735–3756, https://doi.org/10.1175/MWR-D-12-00343.1.

——, S. C. van den Heever, and R. H. Johnson, 2013: Impact of graupel parameterization schemes on idealized bow echo simulations. *Mon. Wea. Rev.*, **141**, 1241–1262, https://doi.org/10.1175/MWR-D-12-00064.1.

Benjamin, S. G., and Coauthors, 2016: A North American hourly assimilation and model forecast cycle: The Rapid Refresh. *Mon. Wea. Rev.*, **144**, 1669–1694, https://doi.org/10.1175/MWR-D-15-0242.1.

Billings, J. M., and M. D. Parker, 2012: Evolution and maintenance of the 22–23 June 2003 nocturnal convection during BAMEX. *Wea. Forecasting*, **27**, 279–300, https://doi.org/10.1175/WAF-D-11-00056.1.

Blackadar, A. K., 1957: Boundary layer wind maxima and their significance for the growth of nocturnal inversions. *Bull. Amer. Meteor. Soc.*, **38**, 283–290, https://doi.org/10.1175/1520-0477-38.5.283.

Blake, B. T., D. B. Parsons, K. R. Haghi, and S. G. Castleberry, 2017: The structure, evolution and dynamics of a nocturnal convective system simulated using the WRF-ARW model. *Mon. Wea. Rev.*, **145**, 3179–3201, https://doi.org/10.1175/MWR-D-16-0360.1.

Bonner, W. D., 1968: Climatology of the low-level jet. *Mon. Wea. Rev.*, **96**, 833–850, https://doi.org/10.1175/1520-0493(1968)096<0833:COTLLJ>2.0.CO;2.

Booker, J. R., and F. P. Bretherton, 1967: The critical layer for internal gravity waves in a shear flow. *J. Fluid Mech.*, **27**, 513–539, https://doi.org/10.1017/S0022112067000515.

Brock, F. V., K. C. Crawford, R. L. Elliott, G. W. Cuperus, S. J. Stadler, H. L. Johnson, and M. D. Eilts, 1995: The Oklahoma Mesonet: A technical overview. *J. Atmos. Oceanic Technol.*, **12**, 5–19, https://doi.org/10.1175/1520-0426(1995)012<0005:TOMATO>2.0.CO;2.

Bryan, G. H., and J. M. Fritsch, 2000: Moist absolute instability: The sixth static stability state. *Bull. Amer. Meteor. Soc.*, **81**, 1207–1230, https://doi.org/10.1175/1520-0477(2000)081<1287:MAITSS>2.3.CO;2.

——, and H. Morrison, 2012: Sensitivity of a simulated squall line to horizontal resolution and parameterization of microphysics. *Mon. Wea. Rev.*, **140**, 202–225, https://doi.org/10.1175/MWR-D-11-00046.1.

Carbone, R. E., and J. D. Tuttle, 2008: Rainfall occurrence in the U.S. warm season: The diurnal cycle. *J. Climate*, **21**, 4132–4146, https://doi.org/10.1175/2008JCLI2275.1.

Carlson, T., S. Benjamin, G. Forbes, and Y. Li, 1983: Elevated mixed layers in the regional severe storm environment: Conceptual model and case studies. *Mon. Wea. Rev.*, **111**, 1453–1474, https://doi.org/10.1175/1520-0493(1983)111<1453:EMLITR>2.0.CO;2.

Chasteen, M. B., 2017: The response of a long-lived mesoscale convective system to changes in lower-tropospheric conditions. M.S. thesis, School of Meteorology, University of Oklahoma, 233 pp.

Christie, D. R., 1989: Long nonlinear waves in the lower atmosphere. *J. Atmos. Sci.*, **46**, 1462–1491, https://doi.org/10.1175/1520-0469(1989)046<1462:LNWITL>2.0.CO;2.

Coniglio, M. C., S. F. Corfidi, and J. S. Kain, 2012: Views on applying RKW theory: An illustration using the 8 May 2009 derecho-producing convective system. *Mon. Wea. Rev.*, **140**, 1023–1043, https://doi.org/10.1175/MWR-D-11-00026.1.

Corfidi, S. F., 2003: Cold pools and MCS propagation: Forecasting the motion of downwind-developing MCSs. *Wea. Forecasting*, **18**, 997–1017, https://doi.org/10.1175/1520-0434(2003)018<0997:CPAMPF>2.0.CO;2.

——, S. J. Corfidi, and D. M. Schultz, 2008: Elevated convection and castellanus: Ambiguities, significance, and questions. *Wea. Forecasting*, **23**, 1280–1303, https://doi.org/10.1175/2008WAF2222118.1.

Crook, N. A., 1988: Trapping of low-level internal gravity waves. *J. Atmos. Sci.*, **45**, 1533–1541, https://doi.org/10.1175/1520-0469(1988)045<1533:TOLLIG>2.0.CO;2.

Crum, T. D., and R. L. Alberty, 1993: The WSR-88D and the WSR-88D operational support facility. *Bull. Amer. Meteor. Soc.*, **74**, 1669–1687, https://doi.org/10.1175/1520-0477(1993)074<1669:TWATWO>2.0.CO;2.

Du, Y., and R. Rotunno, 2014: A simple analytical model of the nocturnal low-level jet over the Great Plains of the United States. *J. Atmos. Sci.*, **71**, 3674–3683, https://doi.org/10.1175/JAS-D-14-0060.1.

Dudhia, J., 1989: Numerical study of convection observed during the Winter Monsoon Experiment using a mesoscale two-dimensional model. *J. Atmos. Sci.*, **46**, 3077–3107, https://doi.org/10.1175/1520-0469(1989)046<3077:NSOCOD>2.0.CO;2.

Ek, M., K. Mitchell, Y. Lin, E. Rogers, P. Grunmann, V. Koren, G. Gayno, and J. Tarpley, 2003: Implementation of Noah land surface model advances in the National Centers for Environmental Prediction operational mesoscale Eta model. *J. Geophys. Res.*, **108**, 8851, https://doi.org/10.1029/2002JD003296.

Fedorovich, E., J. A. Gibbs, and A. Shapiro, 2017: Numerical study of nocturnal low-level jets over gently sloping terrain. *J. Atmos. Sci.*, **74**, 2813–2834, https://doi.org/10.1175/JAS-D-17-0013.1.

French, A. J., and M. D. Parker, 2010: The response of simulated nocturnal convective systems to a developing low-level jet. *J. Atmos. Sci.*, **67**, 3384–3408, https://doi.org/10.1175/2010JAS3329.1.

Fritsch, J., and R. Maddox, 1981: Convectively driven mesoscale weather systems aloft. Part II: Numerical simulations. *J. Appl. Meteor.*, **20**, 20–26, https://doi.org/10.1175/1520-0450(1981)020<0020:CDMWSA>2.0.CO;2.

——, R. Kane, and C. Chelius, 1986: The contribution of mesoscale convective weather systems to the warm-season precipitation in the United States. *J. Climate Appl. Meteor.*, **25**, 1333–1345, https://doi.org/10.1175/1520-0450(1986)025<1333:TCOMCW>2.0.CO;2.

Gale, J. J., W. A. Gallus Jr., and K. A. Jungbluth, 2002: Toward improved prediction of mesoscale convective system dissipation. *Wea. Forecasting*, **17**, 856–872, https://doi.org/10.1175/1520-0434(2002)017<0856:TIPOMC>2.0.CO;2.

Gebauer, J. G., A. Shapiro, E. Fedorovich, and P. Klein, 2018: Convection initiation caused by heterogeneous low-level jets over the Great Plains. *Mon. Wea. Rev.*, **146**, 2615–2637, https://doi.org/10.1175/MWR-D-18-0002.1.

Geerts, B., and Coauthors, 2017: The 2015 Plains Elevated Convection At Night field project. *Bull. Amer. Meteor. Soc.*, **98**, 767–786, https://doi.org/10.1175/BAMS-D-15-00257.1.

Haghi, K. R., D. B. Parsons, and A. Shapiro, 2017: Bores observed during IHOP_2002: The relationship of bores to the nocturnal environment. *Mon. Wea. Rev.*, **145**, 3929–3946, https://doi.org/10.1175/MWR-D-16-0415.1.

Hane, C. E., J. A. Haynes, D. L. Andra Jr., and F. H. Carr, 2008: The evolution of morning convective systems over the U.S. Great Plains during the warm season. Part II: A climatology and the influence of environmental factors. *Mon. Wea. Rev.*, **136**, 929–944, https://doi.org/10.1175/2007MWR2016.1.

Holton, J. R., 1967: The diurnal boundary layer wind oscillation above sloping terrain. *Tellus*, **19**, 199–205, https://doi.org/10.1111/j.2153-3490.1967.tb01473.x.

Horgan, K. L., D. M. Schultz, J. E. Hales Jr., S. F. Corfidi, and R. H. Johns, 2007: A five-year climatology of elevated severe convective storms in the United States east of the Rocky Mountains. *Wea. Forecasting*, **22**, 1031–1044, https://doi.org/10.1175/WAF1032.1.

Houston, A. L., and D. Niyogi, 2007: The sensitivity of convective initiation to the lapse rate of the active cloud-bearing layer. *Mon. Wea. Rev.*, **135**, 3013–3032, https://doi.org/10.1175/MWR3449.1.

Hu, X.-M., and M. Xue, 2016: Influence of synoptic sea-breeze fronts on the urban heat island intensity in Dallas–Fort Worth, Texas. *Mon. Wea. Rev.*, **144**, 1487–1507, https://doi.org/10.1175/MWR-D-15-0201.1.

Janjić, Z., 1996: The surface layer parameterization in the NCEP Eta Model. *Research Activities in Atmospheric and Oceanic Modelling*, CAS/JSC Working Group on Numerical Experimentation, WMO/TD-734, Rep. 23, 4.16–4.17.

Johnson, R. H., and P. J. Hamilton, 1988: The relationship of surface pressure features to the precipitation and airflow structure of an intense midlatitude squall line. *Mon. Wea. Rev.*, **116**, 1444–1473, https://doi.org/10.1175/1520-0493(1988)116<1444:TROSPF>2.0.CO;2.

Kain, J. S., and Coauthors, 2013: A feasibility study for probabilistic convection initiation forecasts based on explicit numerical guidance. *Bull. Amer. Meteor. Soc.*, **94**, 1213–1225, https://doi.org/10.1175/BAMS-D-11-00264.1.

Keene, K. M., and R. S. Schumacher, 2013: The bow and arrow mesoscale convective structure. *Mon. Wea. Rev.*, **141**, 1648–1672, https://doi.org/10.1175/MWR-D-12-00172.1.

Kincer, J. B., 1916: Daytime and nightime precipitation and their economic significance. *Mon. Wea. Rev.*, **44**, 628–633, https://doi.org/10.1175/1520-0493(1916)44<628:DANPAT>2.0.CO;2.

Knupp, K., 2006: Observational analysis of a gust front to bore to solitary wave transition within an evolving nocturnal boundary layer. *J. Atmos. Sci.*, **63**, 2016–2035, https://doi.org/10.1175/JAS3731.1.

Koch, S. E., and W. L. Clark, 1999: A nonclassical cold front observed during COPS-91: Frontal structure and the process of severe storm initiation. *J. Atmos. Sci.*, **56**, 2862–2890, https://doi.org/10.1175/1520-0469(1999)056<2862:ANCFOD>2.0.CO;2.

——, P. B. Dorian, R. Ferrare, S. Melfi, W. C. Skillman, and D. Whiteman, 1991: Structure of an internal bore and dissipating gravity current as revealed by Raman lidar. *Mon. Wea. Rev.*, **119**, 857–887, https://doi.org/10.1175/1520-0493(1991)119<0857:SOAIBA>2.0.CO;2.

——, W. Feltz, F. Fabry, M. Pagowski, B. Geerts, K. M. Bedka, D. O. Miller, and J. W. Wilson, 2008a: Turbulent mixing processes in atmospheric bores and solitary waves deduced from profiling systems and numerical simulation. *Mon. Wea. Rev.*, **136**, 1373–1400, https://doi.org/10.1175/2007MWR2252.1.

——, C. Flamant, J. W. Wilson, B. M. Gentry, and B. D. Jamison, 2008b: An atmospheric soliton observed with Doppler radar, differential absorption lidar, and a molecular Doppler lidar. *J. Atmos. Oceanic Technol.*, **25**, 1267–1287, https://doi.org/10.1175/2007JTECHA951.1.

Lindzen, R., and K. Tung, 1976: Banded convective activity and ducted gravity waves. *Mon. Wea. Rev.*, **104**, 1602–1617, https://doi.org/10.1175/1520-0493(1976)104<1602:BCAADG>2.0.CO;2.

Maddox, R. A., 1980: Meoscale convective complexes. *Bull. Amer. Meteor. Soc.*, **61**, 1374–1387, https://doi.org/10.1175/1520-0477(1980)061<1374:MCC>2.0.CO;2.

——, 1983: Large-scale meteorological conditions associated with midlatitude, mesoscale convective complexes. *Mon. Wea. Rev.*, **111**, 1475–1493, https://doi.org/10.1175/1520-0493(1983)111<1475:LSMCAW>2.0.CO;2.

Mahoney, K. M., and G. M. Lackmann, 2011: The sensitivity of momentum transport and severe surface winds to environmental moisture in idealized simulations of a mesoscale convective system. *Mon. Wea. Rev.*, **139**, 1352–1369, https://doi.org/10.1175/2010MWR3468.1.

——, ——, and M. D. Parker, 2009: The role of momentum transport in the motion of a quasi-idealized mesoscale convective system. *Mon. Wea. Rev.*, **137**, 3316–3338, https://doi.org/10.1175/2009MWR2895.1.

Marsham, J. H., S. B. Trier, T. M. Weckwerth, and J. W. Wilson, 2011: Observations of elevated convection initiation leading to a surface-based squall line during 13 June IHOP_2002. *Mon. Wea. Rev.*, **139**, 247–271, https://doi.org/10.1175/2010MWR3422.1.

Means, L. L., 1952: On thunderstorm forecasting in the central United States. *Mon. Wea. Rev.*, **80**, 165–189, https://doi.org/10.1175/1520-0493(1952)080<0165:OTFITC>2.0.CO;2.

Mlawer, E. J., S. J. Taubman, P. D. Brown, M. J. Iacono, and S. A. Clough, 1997: Radiative transfer for inhomogeneous atmospheres: RRTM, a validated correlated-k model for the longwave. *J. Geophys. Res.*, **102**, 16 663–16 682, https://doi.org/10.1029/97JD00237.

Moore, J. T., F. H. Glass, C. E. Graves, S. M. Rochette, and M. J. Singer, 2003: The environment of warm-season elevated thunderstorms associated with heavy rainfall over the central United States. *Wea. Forecasting*, **18**, 861–878, https://doi.org/10.1175/1520-0434(2003)018<0861:TEOWET>2.0.CO;2.

Morrison, H., G. Thompson, and V. Tatarskii, 2009: Impact of cloud microphysics on the development of trailing stratiform precipitation in a simulated squall line: Comparison of one- and two-moment schemes. *Mon. Wea. Rev.*, **137**, 991–1007, https://doi.org/10.1175/2008MWR2556.1.

Nakanishi, M., and H. Niino, 2006: An improved Mellor–Yamada level-3 model: Its numerical stability and application to a regional prediction of advection fog. *Bound.-Layer Meteor.*, **119**, 397–407, https://doi.org/10.1007/s10546-005-9030-8.

——, and ——, 2009: Development of an improved turbulence closure model for the atmospheric boundary layer. *J. Meteor. Soc. Japan*, **87**, 895–912, https://doi.org/10.2151/jmsj.87.895.

Nicholls, M. E., R. A. Pielke, and W. R. Cotton, 1991: Thermally forced gravity waves in an atmosphere at rest. *J. Atmos. Sci.*, **48**, 1869–1884, https://doi.org/10.1175/1520-0469(1991)048<1869:TFGWIA>2.0.CO;2.

Nowotarski, C. J., P. M. Markowski, and Y. Richardson, 2011: The characteristics of numerically simulated supercell storms situated over statically stable boundary layers. *Mon. Wea. Rev.*, **139**, 3139–3162, https://doi.org/10.1175/MWR-D-10-05087.1.

Parker, M. D., 2008: Response of simulated squall lines to low-level cooling. *J. Atmos. Sci.*, **65**, 1323–1341, https://doi.org/10.1175/2007JAS2507.1.

Parsons, D. B., K. R. Haghi, K. T. Halbert, B. Elmer, and J. Wang, 2019: The potential role of atmospheric bores and gravity waves in the initiation and maintenance of nocturnal convection over the Southern Great Plains. *J. Atmos. Sci.*, **76**, 43–68, https://doi.org/10.1175/JAS-D-17-0172.1.

Peters, J. M., and R. S. Schumacher, 2015: Mechanisms for organization and echo training in a flash-flood-producing mesoscale convective system. *Mon. Wea. Rev.*, **143**, 1058–1085, https://doi.org/10.1175/MWR-D-14-00070.1.

Pinto, J. O., J. A. Grim, and M. Steiner, 2015: Assessment of the High-Resolution Rapid Refresh models ability to predict mesoscale convective systems using object-based evaluation.

Wea. Forecasting, **30**, 892–913, https://doi.org/10.1175/WAF-D-14-00118.1.

Pu, B., and R. E. Dickinson, 2014: Diurnal spatial variability of Great Plains summer precipitation related to the dynamics of the low-level jet. *J. Atmos. Sci.*, **71**, 1807–1817, https://doi.org/10.1175/JAS-D-13-0243.1.

Reif, D. W., and H. B. Bluestein, 2017: A 20-year climatology of nocturnal convection initiation over the central and southern Great Plains during the warm season. *Mon. Wea. Rev.*, **145**, 1615–1639, https://doi.org/10.1175/MWR-D-16-0340.1.

Rottman, J. W., and J. E. Simpson, 1989: The formation of internal bores in the atmosphere: A laboratory model. *Quart. J. Roy. Meteor. Soc.*, **115**, 941–963, https://doi.org/10.1002/qj.49711548809.

Rotunno, R., J. B. Klemp, and M. L. Weisman, 1988: A theory for strong, long-lived squall lines. *J. Atmos. Sci.*, **45**, 463–485, https://doi.org/10.1175/1520-0469(1988)045<0463:ATFSLL>2.0.CO;2.

Schumacher, R. S., 2009: Mechanisms for quasi-stationary behavior in simulated heavy-rain-producing convective systems. *J. Atmos. Sci.*, **66**, 1543–1568, https://doi.org/10.1175/2008JAS2856.1.

——, 2015: Sensitivity of precipitation accumulation in elevated convective systems to small changes in low-level moisture. *J. Atmos. Sci.*, **72**, 2507–2524, https://doi.org/10.1175/JAS-D-14-0389.1.

——, and R. H. Johnson, 2005: Organization and environmental properties of extreme-rain-producing mesoscale convective systems. *Mon. Wea. Rev.*, **133**, 961–976, https://doi.org/10.1175/MWR2899.1.

Scorer, R., 1949: Theory of waves in the lee of mountains. *Quart. J. Roy. Meteor. Soc.*, **75**, 41–56, https://doi.org/10.1002/qj.49707532308.

Shapiro, A., and E. Fedorovich, 2009: Nocturnal low-level jet over a shallow slope. *Acta Geophys.*, **57**, 950–980, https://doi.org/10.2478/s11600-009-0026-5.

——, ——, and S. Rahimi, 2016: A unified theory for the Great Plains nocturnal low-level jet. *J. Atmos. Sci.*, **73**, 3037–3057, https://doi.org/10.1175/JAS-D-15-0307.1.

Skamarock, W., and Coauthors, 2008: A description of the Advanced Research WRF version 3. NCAR Tech. Note NCAR/TN-475+STR, 113 pp., https://doi.org/10.5065/D68S4MVH.

Song, J., K. Liao, R. L. Coulter, and B. M. Lesht, 2005: Climatology of the low-level jet at the southern Great Plains atmospheric boundary layer experiments site. *J. Appl. Meteor.*, **44**, 1593–1606, https://doi.org/10.1175/JAM2294.1.

Surcel, M., M. Berenguer, and I. Zawadzki, 2010: The diurnal cycle of precipitation from continental radar mosaics and numerical weather prediction models. Part I: Methodology and seasonal comparison. *Mon. Wea. Rev.*, **138**, 3084–3106, https://doi.org/10.1175/2010MWR3125.1.

Thompson, R. L., B. T. Smith, J. S. Grams, A. R. Dean, and C. Broyles, 2012: Convective modes for significant severe thunderstorms in the contiguous United States. Part II: Supercell and QLCS tornado environments. *Wea. Forecasting*, **27**, 1136–1154, https://doi.org/10.1175/WAF-D-11-00116.1.

Toms, B. A., J. M. Tomaszewski, D. D. Turner, and S. E. Koch, 2017: Analysis of a gravity wave train using direct and remote sensing measurement systems. *Mon. Wea. Rev.*, **145**, 2791–2812, https://doi.org/10.1175/MWR-D-16-0216.1.

Trier, S. B., and D. B. Parsons, 1993: Evolution of environmental conditions preceding the development of a nocturnal mesoscale convective complex. *Mon. Wea. Rev.*, **121**, 1078–1098,

https://doi.org/10.1175/1520-0493(1993)121<1078:EOECPT> 2.0.CO;2.

——, J. H. Marsham, C. A. Davis, and D. A. Ahijevych, 2011: Numerical simulations of the postsunrise reorganization of a nocturnal mesoscale convective system during 13 June IHOP_2002. *J. Atmos. Sci.*, **68**, 2988–3011, https://doi.org/10.1175/JAS-D-11-0112.1.

Wakimoto, R. M., P. Stauffer, and W.-C. Lee, 2015: The vertical vorticity structure within a squall line observed during BAMEX: Banded vorticity features and the evolution of a bowing segment. *Mon. Wea. Rev.*, **143**, 341–362, https://doi.org/10.1175/MWR-D-14-00246.1.

Wallace, M. J., 1975: Diurnal variations in precipitation and thunderstorm frequency over the conterminous United States. *Mon. Wea. Rev.*, **103**, 406–419, https://doi.org/10.1175/1520-0493(1975)103<0406:DVIPAT>2.0.CO;2.

Weisman, M. L., 1992: The role of convectively generated rear-inflow jets in the evolution of long-lived mesoconvective systems. *J. Atmos. Sci.*, **49**, 1826–1847, https://doi.org/10.1175/1520-0469(1992)049<1826:TROCGR>2.0.CO;2.

——, 1993: The genesis of severe, long-lived bow echoes. *J. Atmos. Sci.*, **50**, 645–670, https://doi.org/10.1175/1520-0469(1993)050<0645:TGOSLL>2.0.CO;2.

——, and C. A. Davis, 1998: Mechanisms for the generation of mesoscale vortices within quasi-linear convective systems. *J. Atmos. Sci.*, **55**, 2603–2622, https://doi.org/10.1175/1520-0469(1998)055<2603:MFTGOM>2.0.CO;2.

Whiteman, C. D., X. Bian, and S. Zhong, 1997: Low-level jet climatology from enhanced rawinsonde observations at a site in the southern Great Plains. *J. Appl. Meteor. Climatol.*, **36**, 1363–1376, https://doi.org/10.1175/1520-0450(1997)036<1363:LLJCFE>2.0.CO;2.

Wilson, J. W., and R. D. Roberts, 2006: Summary of convective storm initiation and evolution during IHOP: Observational and modeling perspective. *Mon. Wea. Rev.*, **134**, 23–47, https://doi.org/10.1175/MWR3069.1.